# Development of Actuator and Force Sensor For Small-Scale Mechanical Testing

by

Gökhan Nadar

A Thesis Submitted to the
Graduate School of Engineering
in Partial Fulfillment of the Requirements for
the Degree of

Master of Science
in
Mechanical Engineering

Koc University

September 2013

Koc University

Graduate School of Sciences and Engineering

This is to certify that I have examined this copy of a master's thesis by

Gökhan Nadar

and have found that it is complete and satisfactory in all respects,

and that any and all revisions required by the final

examining committee have been made.

Committee Members:

________________________________________

B. Erdem Alaca, Ph. D. (Advisor)

________________________________________

Arda D. Yalçınkaya, Ph. D.

________________________________________

Göksenin Yaralıoğlu, Ph. D.

Date: ____________________________

*To my dear family*

## ABSTRACT

This study is geared towards providing a uniaxial tension test platform for silicon nanowires, which includes an actuator, a force sensor and a single Si nanowire as the sample. Actuator pulls the Si nanowire at one of its tips, whereas the force acting on the Si nanowire is traced by the sensor attached at the opposing tip of the Si nanowire. The whole assembly is intended to be fabricated monolithically to overcome sample/device alignment and interface issues. This study reports design, fabrication and characterization of MEMS actuators and force sensors to meet the needs of such a testing platform.

A set of four electrostatic actuators and four tri-plate force sensors based on differential capacitive readout are designed for Si nanowires of different sizes. Actuators are designed to generate forces ranging from 3 μN to 32 μN to enable the fracture of each Si nanowire while having a maximum actuation voltage of 10V - 25V. The minimum obtained ratio of the horizontal pull-in voltage to the actuation voltage is 2.6 for this set of actuators. Force sensors are designed to have a measurement range from 1.0 μN to 28.5 μN corresponding to the onset of fracture in Si nanowires. Sensitivity values, taken as the ratio of readout voltage to Si nanowire strain, are obtained as 0.65, 3.26, 5.46 and 3.74 V/(μm/μm). The corresponding displacement ranges of the sensors are in the submicron region ranging from 0.209 μm to 0.377 μm. Furthermore, non-linearity of the sensors is designed to be less than %5.

First-generation actuator fabrication is accomplished through surface micromachining of SOI wafers with 10 μm device layer, 1 μm BOX layer and 380 μm handle layer, whereas force sensor fabrication failed during final release step of backside etching of the handle layer. To prevent the failure, we foresee the usage of a protective and conformal material which will enhance the rigidity of the device and will be removed easily after etching. Characterization of the first-generation actuators is accomplished by

carrying out CV measurements. Results indicate that MOS capacitance is dominant over MEMS capacitance. The following conclusions are drawn based on fabrication and characterization of the first-generation actuators, which are taken into account in the design phase of the new set of devices, whose specifications were indicated above.

1. Release of actuators is problematic. A back-side etch is necessary;
2. A protective and conformal material is necessary for back-side etching;
3. With decreasing displacement values, MOS capacitance effect becomes increasingly important and has to be taken into account in the electromechanical design.

## ÖZET

Bu çalışma, Silisyum nanoteller için tek eksenli bir çekme testi platformu sağlamak amacıyla yürütülmüştür. Bu platform, bir eyleyici, bir kuvvet algılayıcısı ve numune olarak tek bir Silisyum nanotelden oluşmaktadır. Eyleyici, Silisyum nanoteli bir ucundan çekerken, Silisyum nanotelin diğer ucuna bağlı algılayıcı numune üzerine etkiyen kuvveti ölçer. Tüm sistem, hem numune/cihaz hizalaması hem arayüz problemlerini bertaraf etmek için monolitik olarak üretilecektir. Bu çalışmada, bu tür bir test platformunun ihtiyaçlarını karşılayacak bir MEMS eyleyici ve kuvvet algılayıcısının tasarım, imalat ve karakterizasyonu anlatılmıştır.

Değişik boyutlu Silisyum nanotellere yönelik olarak, dört farklı elektrostatik eyleyici ve yine dört farklı, üç plakalı ve sığa değişimini ölçmeye dayalı kuvvet algılayıcısı tasarlanmıştır. Silisyum nanotelleri kıracak şekilde, 3 µN ila 32 µN arasında değişen kuvvet aralığında çalışan eyleyicilerin en yüksek tahrik potansiyeli 10V ile 25V arasında değişmektedir. Elde edilen en düşük "pull-in" / tahrik potansiyeli oranı 2.6'dır. Kuvvet algılayıcıları, Silisyum nanotellerin kırılması için 1.0 µN ila 28.5 µN arasında değişen kuvvet aralıklarında çalışmak üzere tasarlanmıştır. Algılayıcının çıkış potansiyelinin Silisyum nanoteldeki gerinime oranı olarak tanımlanan algılayıcı hassasiyeti ise söz konusu dört tasarımda 0.65, 3.26, 5.46 ve 3.74 V/(µm/µm) olarak belirlenmiştir. Bu değerlere karşılık gelen algılayıcı yer değiştirme aralıkları ise, 0.209 µm ila 0.377 µm arasında değişmektedir. Algılayıcıların doğrusallıktan sapışları %5 değerinin altında tutulmuştur.

Birinci nesil eyleyici üretimleri 10 µm cihaz katmanı, 1 µm BOX katmanı ve 380 µm alttaş katmanı olan SOI'lar kullanılarak gerçekleştirilmiştir. Kuvvet algılayıcıları ise alttaş katmanının Silisyum aşındırması esnasında kırılmışlardır. Sonraki üretimlerde bu durumu engellemek için, koruyucu ve konformal bir mazleme kullanımı önerilmektedir. Bu malzeme kolay kaldırılabilir olmakla birlikte, cihazların rijiditesini muhafaza etmesini

sağlayacaktır. Birinci nesil eyleyici karakterizasyonu sığa - tahrik potansiyeli ölçümleri ile tamamlanmıştır. Sonuçlara göre, metal-oksit-yarı iletken sığası, MEMS sığasına göre baskın davranmaktadır. Birinci nesil eyleyici tasarımları için yapılan üretim ve karaterizasyon adımlarından çıkan aşağıdaki sonuçlar dikkate alınarak, yukarıda özellikleri belirtilmiş olan yeni nesil eyleyici ve kuvvet algılayıcıları tasarlanmıştır.

1. Eyleyici üretiminde BOX katmanının tamamen kaldırılması sorunlu durumdadır. Alttaş katmanı Silisyum aşındırması gerekmektedir.

2. Alttaş katmanı Silisyum aşındırması için koruyucu ve konformal bir malzeme gerekmektedir.

3. Yer değiştirme miktarlarının düşmesi ile, metal-oksit-yarı iletken sığa etkisi daha önemli bir hale gelmekte ve elektromekanik tasarım sırasında dikkate alınması gerekmektedir.

## ACKNOWLEDGEMENTS

I would like to present my extreme gratitude to Dr. B. Erdem Alaca for accepting me as a part of his great research group, giving me an opportunity to work at EPFL whose facilities are one of a kind and more importantly behaving as a father throughout my undergraduate and graduate years. I also would like to thank Dr. Yusuf Leblebici for inviting and providing me wonderful working environment in LSM-EPFL.

I am indebted to Dr. Arda D. Yalçınkaya for all of his guidance and endless efforts throughout characterization steps carried out in Boğaziçi University and participating as a committee member in my thesis defense. His laboratory, Micro Nano Characterization Lab., provided me the most beneficial equipments to finalize characterizations.

I am very grateful to Dr. Göksenin Yaralıoğlu for acting as a committee member in my thesis defense.

I am thankful to CMi-EPFL members for all their support during fabrication and BETA-Boğaziçi University members for their enthusiasm.

Lastly, I owe a lot to Merve Burtaçgiray bringing the joy of life to me and completing my other half, to my friends especially Yusuf Aydın being a great friend and more than a brother for the last 11 years of my life and to Mechanical Characterization Lab. members for helping me at hard conditions.

This study is supported by Tübitak under Grant No: 112E058 and by Koç University - İstanbul Rotary Club Fundamental Research Seed Fund Program.

## TABLE OF CONTENTS

**List of Tables** xii

**List of Figures** xiii

**Chapter 1: Introduction** 1

**Chapter 2: Actuator Modeling and Design** 6

2.1 System Overview 6

2.2 Design Algorithm 8

2.2.1 Formulas 9

2.2.2 Design Criteria 11

2.2.2.1 Device Simplicity 11

2.2.2.2 Device Stability 11

2.2.2.3 Device Linearity 13

2.3 Design Output Parameters 14

**Chapter 3: Force Sensor Modeling and Design** 16

3.1 System Overview 16

3.2 Design Algorithm 19

3.2.1 Formulas 20

3.2.2 Design Criteria 24

3.2.2.1 Force and Displacement Data for Fracture 24

3.2.2.2 Device Simplicity 24

3.2.2.3 Device Stability 25
3.2.2.3.1 Fringing Field 25
3.2.2.3.2 Pull-in 25
3.2.2.3.3 Nonlinearity Due to Force 25
3.2.2.3.4 Finger Bending Due to Electrostatic Force 26
3.2.2.3.5 Readout Voltage Correction 26
3.2 Design Force Sensor Parameters 26

**Chapter 4: Fabrication 31**
4.1 Chrome Mask Fabrication 31
4.2 Chrome Mask Fabrication 31
4.3 Actuator Fabrication 32
4.3.1 HMDS and Photoresist Coating 33
4.3.2 Photolithography 33
4.3.3 Development 33
4.3.4 SRD and Device Layer Si Etch 34
4.3.5 Photoresist Removal and Scribing 34
4.3.6 BOX Removal 34
4.3.7 Cr-Au Coating 35
4.4 Force Fabrication 36
4.4.5 Photoresist Strip 37
4.4.6 Handle Layer Photoresist Coating 37
4.4.7 Handle Layer Photolithography 37
4.4.8 Handle Layer Development 38
4.4.9 SRD and Handle Layer Si Etch 38
4.4.10 Handle Layer Photoresist Strip and Scribing 39

4.4.11 BOX Removal 39
4.4.12 Cr-Au Coating 39

**Chapter 5: Characterization 41**
5.1 Actuator Characterization 41
5.1.1 Setup 41
5.1.2 Measurements 43
5.2 Force Sensor Characterization 46

**Chapter 6: Parasitic Effects 48**
6.1 Introduction 48
6.2 Background 48
6.3 Effect in Our Project 50

**Chapter 7: Conclusion and Future Work 54**

**Appendix A: MATLAB Code of Actuator and Force Sensor 56**
**Appendix B: SEM Images of Fabricated Actuators and Test Wafer Characterizations 75**
**Appendix C: CV Characterization Plots of Actuators 83**
**Appendix D: 2-D Simulations 85**

**Bibliography 89**
**Vita 91**

## LIST OF TABLES

Table 1.1 Sample specifications 4

Table 2.1 First-generation actuator design parameters 14
Table 2.2 New-generation actuator design parameters 14

Table 3.1 First-generation force sensor design parameters 26
Table 3.2 New-generation force sensor design parameters 30

## LIST OF FIGURES


| | | |
|---|---|---|
| Figure 1.1: | Mass-spring model of a micro tensile testing device | 2 |
| Figure 1.2: | Electrostatic comb-drive actuator, Si nanowire and triplate force sensor representation | 4 |
| Figure 2.1: | Single combd-drive finger schematic | 7 |
| Figure 2.2: | Actuator design algorithm | 8 |
| Figure 2.3: | A: Horizontal displacement of movable fingers, B: Vertical displacement of movable fingers | 12 |
| Figure 3.1: | Force sensor schematic | 17 |
| Figure 3.2: | Capacitances on force sensor | 18 |
| Figure 3.3: | Force sensor design algortihm | 19 |
| Figure 3.4: | Finger bending due to electrostatic force | 22 |
| Figure 3.5: | Electrical model of force sensor having no MOS effect | 27 |
| Figure 3.6: | Electrical model of force sensor including MOS effect | 28 |
| Figure 4.1: | Fabrication process flow for actuator | 32 |
| Figure 4.2: | SEM picture of a fabricated actuator | 35 |
| Figure 4.3: | Fabrication process flow for force sensor | 36 |
| Figure 5.1: | Capacitance measurement setup for actuator | 41 |
| Figure 5.2: | Low current - low potential and high current - high potential connection | 42 |
| Figure 5.3: | Capacitance - voltage measurement of device 2A2-A1 at 1MHz | 43 |
| Figure 5.4: | Capacitance - voltage measurement of device 3A3-A1 at 1MHz | 44 |
| Figure 5.5: | Capacitance - voltage measurement of device 4A4-1 at 1MHz | 45 |
| Figure 5.6: | Resonance frequency measurement setup for force sensor | 46 |
| Figure 5.7: | Force sensor readout voltage measurement schematic | 47 |
| Figure 6.1: | MOS capacitance representation and electrical model | 48 |
| Figure 6.2: | Gate voltage - capacitance of an n-type MOS capacitor | 49 |
| Figure 6.3: | Actuator CV measurement schematic | 51 |
| Figure 6.4: | A: Electrical model of first assumption including only MEMS capacitance, B: Revised electrical model with MOS capacitance effect | 51 |

Figure 6.5: EDS analysis result of the SOI wafer used for fabrication 53

Figure 7.1: Revised fabrication process flow for actuator and force sensor 55

# Chapter 1

# INTRODUCTION

Small-scale mechanical and electrical property testing for materials, especially for Si, are gaining importance. Size affect observed in properties of Si such as thermal conductivity, electrical resistivity, piezoresistance, bending strength and modulus of elasticity is of both of scientific and technological interest. At the same time there is a considerable variation in measurements – especially in mechanical properties- reported by different research groups. Therefore, more reliable measurement techniques should be introduced for small-scale material testing.

Mechanical testing of Si is carried out through two main techniques: bending test [1, 2, 3, 4, 5, 6, 7] and tensile test [8, 9, 10, 11, 12, 13, 14, 15, 16, 17]. Bending test is conducted with a single or double clamped beam and an Atomic Force Microscopy (AFM) tip. AFM tip bends the sample in a specific orientation and causes deflection. On the other hand, tensile testing relies on MEMS based actuation and sensing mechanism. However, issues related to the bending test are reported in [18, 19] as follows.

- The displacements are higher in bending tests providing easier detection of deflection. On the other hand, force required to create same stress levels on the specimen is much smaller for bending test which is in need of a higher resolution for force sensing.
- Variations in sample geometry and sample/device alignment pose a greater difficulty in bending test.

- Bending tests are more complicated due to large-deformation-behavior and stress concentration phenomenon at the loading point. Hence, complete modeling of the bending test is required for reliable characterization.

In tensile testing, specimen undergoes a longitudinal force to be stretched. Amount of elongation is measured via optical [14, 17] or capacitive reading [8, 11, 12, 16]. Testing platform mainly consists of three parts: an actuator, a sample and a sensor. In Figure 1.1, a representative mass-spring model of whole system is demonstrated. Actuator and force sensor working principles and design parameters will be discussed in detail in Chapter 2 and 3.

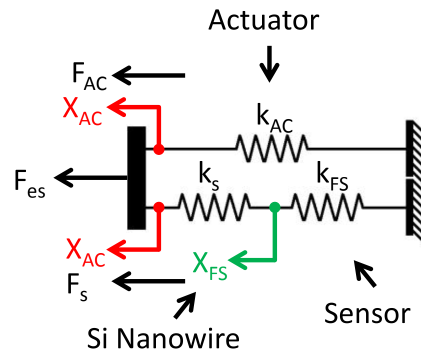


**Figure 1.1**: Mass-spring model of a micro tensile testing device. $F_{es}$ is generated electrostatic force, $F_{AC}$ is force on actuator springs, $x_{AC}$ is actuator displacement, $F_s$ is force on the sample, $x_{FS}$ is force sensor displacement, $k_{FS}$ is force sensor spring constant, $k_s$ is sample spring constant and $k_{AC}$ is actuator spring constant

Mainly two types of actuation mechanism are utilized for tensile testing: electrostatic actuation and thermal actuation. In this project comb-drive electrostatic actuation is preferred over thermal actuation for [19]:

- being less dependent on fabrication process,
- providing large displacement ranges,

- having no requirement for heating,
- generating highly in-plane forces easier.

As for the bending test, small scale tensile testing has its own problems [20].

- Integration of the sample with the testing device,
- Creation of small forces and detection of small displacements at nanoNewton (nN) and nanometer (nm) scales,
- The effect of friction and machine compliance.

In this study micro tensile testing is employed. A representative drawing of the proposed testing platform is given in Figure 1.2. We foresee suggestions for the issues related to tensile testing as follows.

- *Problem 1: Integration of the sample with the testing device*. Suggestion: monolithic on-chip fabrication of actuator, sample and sensor will prevent integration related problems.
- *Problem 2: Creation of small forces and detection of small displacements at nanoNewton (nN) and nanometer (nm) scales*. Suggestion: use of comb-drive actuation and tri-plate differential capacitive reading.
- *Problem 3: The effect of friction and machine compliance.* Suggestion: monolithic on-chip fabrication prevents interfacial reactions. Also, spring optimization for actuator, sample and sensor will overcome machine compliance.
- *Problem 4: The need for extensive modeling to convert measured forces to actual stresses in the sample*. Straightforward conversion thanks to uniaxial stress state and lack of contact.

Nanowires are chosen as the sample geometry, as one can easily change their surface-to-volume ratio and sample volume. We have four different actuators and four different sensors for four different Si nanowires listed in Table 1.1. In this table, required

fracture force values are given as well. A conservative assumption of a fracture strength of 12 GPa is made [2] for the purpose of calculation of these forces.

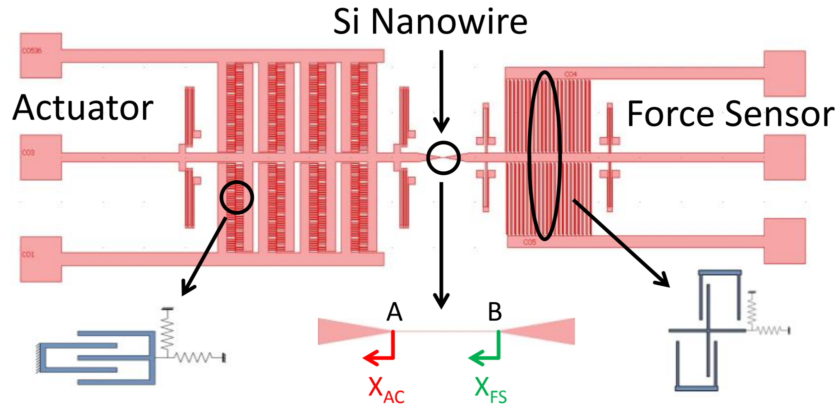


**Figure 1.2:** Electrostatic comb-drive actuator, Si nanowire and tri-plate force sensor representation. Points A and B are connection points of Si nanowire to actuator and force sensor

**Table 1.1** Sample Specifications

| Sample | Sample Volume ($nm^3$) | Diameter ($d_s$) (nm) | Length ($l_s$) (nm) | Fracture Force (μN) |
|---|---|---|---|---|
| Nanowire 1 | $10^4$ | 10 | 127 | 0.94 |
| Nanowire 2 | $10^5$ | 20 | 320 | 3.77 |
| Nanowire 3 | $10^6$ | 32 | 1280 | 9.65 |
| Nanowire 4 | $10^7$ | 55 | 4209 | 28.51 |

This study reports on the development of actuator and force sensors for small scale tensile testing of silicon nanowires. It is a continuation of previous work by Arkan [21] and Gumus [22]. Arkan reported parametrical analysis for force sensor to create a guideline and Gumus has contributed by designing and characterizing a specific actuator and force sensor geometry for a Si nanowire with 75 nm diameter and 30 μm length. Devices were

fabricated by using SOI (Silicon-on-insulator) having 50 µm Si (Silicon) device layer, 2 µm BOX (Buried $SiO_2$-Silicondioxide-) and 380 µm Si handle layer in Center of MicroNano Technology (CMi), EPFL. These devices were found to have pull-in at around 9V of actuation voltage. Also, having 50 µm device layer thickness is a risk for monolithic fabrication in the future. Preserving a single nanowire having diameter values from 10 nm to 50 nm during a 50 µm Si etch is not reasonable so that we introduce the use of SOI wafers having 10 µm Si device layer and 1 µm of BOX layer.

In the remainder of this thesis we report methodology, design criteria, first and new generation design geometries for actuators in Chapter 2. Also, methodology, design criteria, first and new generation design geometries for force sensors are introduced in Chapter 3. In Chapter 4, fabrication process flows for actuators and force sensors are described individually. During first generation force sensor fabrication, SOI wafer cracked due to enormous intrinsic stress inside of it. Additional process steps for force sensor fabrication are proposed as well. First generation fabrication of our designed actuators resulted with the existence of parasitic effects at the characterization step carried out at Micro Nano Characterization Lab, Boğaziçi University (see Chapter 5). Hence, MOS capacitance was modeled for better a design as described in Chapter 6.

# Chapter 2

# ACTUATOR MODELLING AND DESIGN

## 2.1 System Overview

Actuator is the force generator of whole device. Its working principle simply depends on comb drive actuation electrostatically. A representative schematic is shown in Figure 2.1. Voltage is applied to the comb fingers attached to the fixed walls and comb fingers attached to the moving shuttle is set to ground. Electric field is generated between the fingers and therefore capacitance. Changing the voltage value at fixed part changes the electrostatic energy (W) (Equation (2.1). Electrostatic force is simply derived from energy as in Equation (2.3) and in a loop while the voltage changes, capacitance and electrostatic force keep changing so that shuttle moves towards fixed fingers Equations (2.2) and (2.3).

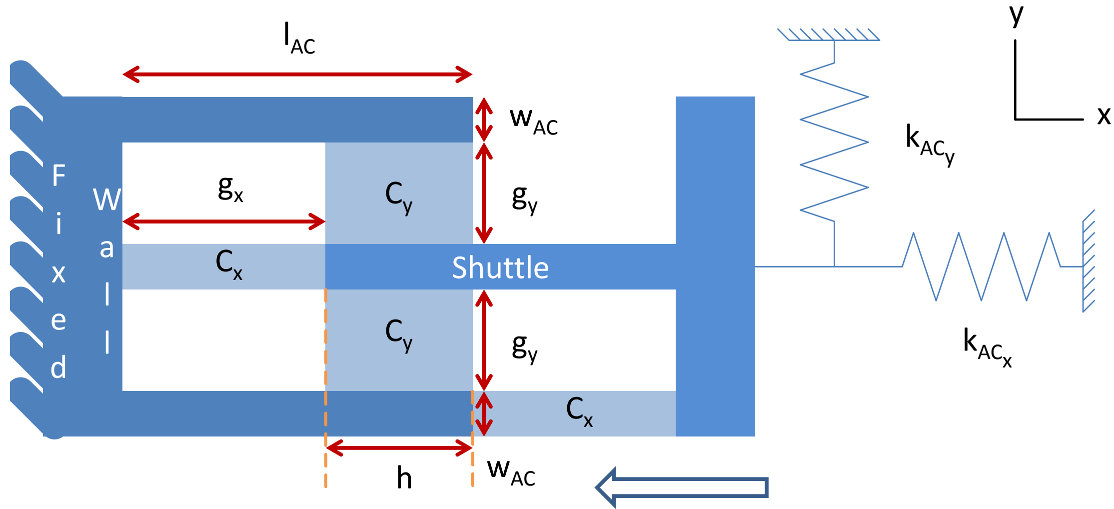


**Figure 2.1**: Single comb-drive finger schematic. $g_x$ is horizontal between wall and finger, $g_y$ is vertical distance between comb fingers, $w_{AC}$ is actuator finger width, "h" is the finger overlap, $k_{ACy}$ is the actuator spring constant in y direction, $k_{ACx}$ is the actuator spring constant in x direction. [23]

$$W = \frac{1}{2} C V^2 \tag{2.1}$$

$$C = \frac{\varepsilon A}{d} = 2C_x + 2C_y = 2N_{AC}\varepsilon_0 t \left[ \frac{w_{AC}}{g_x - x} - \frac{(h + x)}{g_y} \right] \tag{2.2}$$

$$F_{es} = \frac{\partial W}{\partial x} = \frac{1}{2}\frac{\partial C}{\partial x} V^2 = \mathrm{N_{AC}} \varepsilon_0 \mathrm{t} \left[ \frac{\mathrm{w_{AC}}}{(\mathrm{g_x} - \mathrm{x})^2} + \frac{1}{\mathrm{g_y}} \right] V^2 \tag{2.3}$$

In Equation (2.2) and Equation (2.3), "A" is the overlapping area that is responsible for capacitance generation. $N_{AC}$ is the number of fingers for actuator. "V" is the potential difference between fixed and moving fingers and "x" is the amount of finger displacement.

## 2.2. Design Algorithm

In this project, actuator design is carried out with an algorithm as outlined in Figure 2.2. We reach the final geometry values by applying specific formulas, which are explained in later subtitles, by using sample and wafer material specifications and some relating data regarding sensor and actuator.

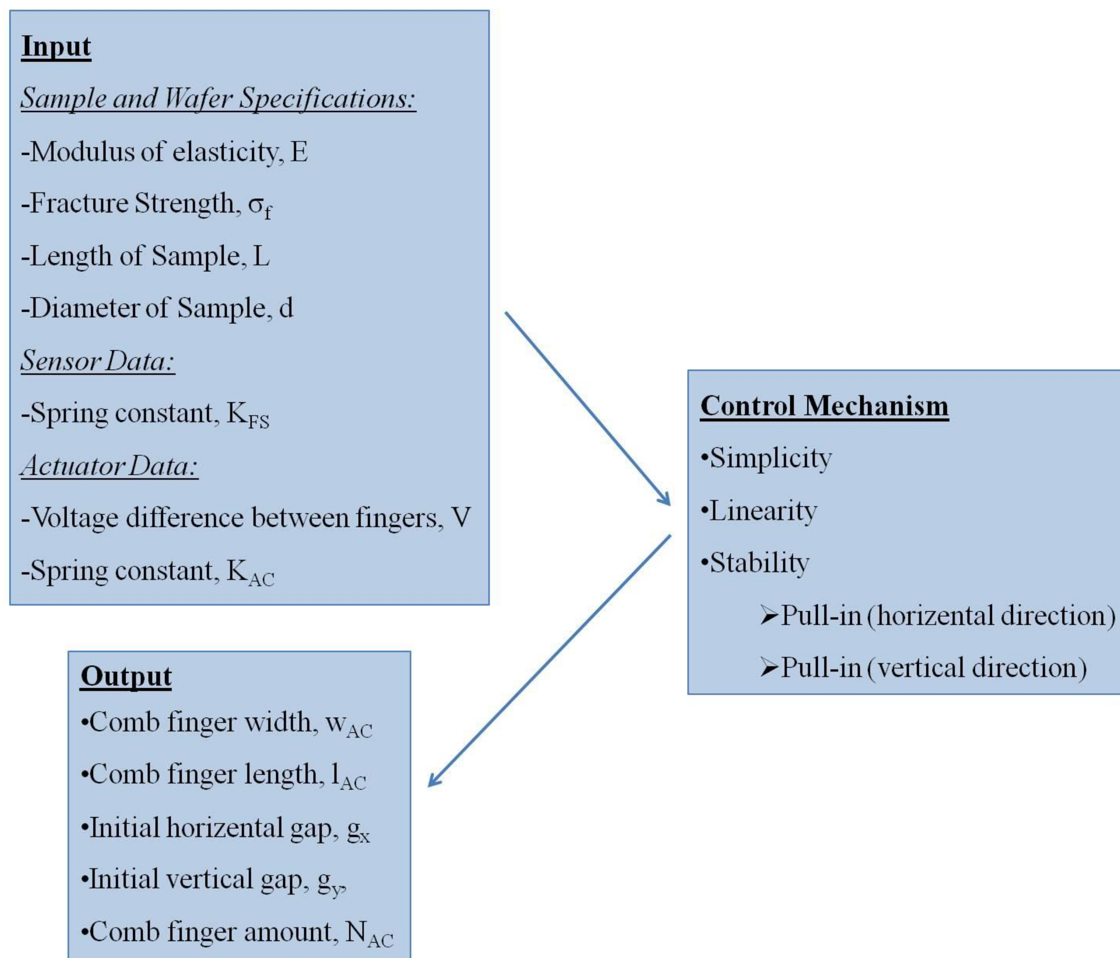


**Figure 2.2**: Actuator design algorithm

### 2.2.1. Formulations

Design parameters are found via a MATLAB environment having below formulas. Si material specifications (modulus of elasticity and fracture strength), desired Si nanowire dimensions (length and diameter), device layer thickness of SOI (Silicon-on-insulator) wafer are encoded at once. Device layer thickness of SOI will serve as actuator thickness.

By using Equation (2.4), force required for fracture of Si nanowire is calculated due to desired dimensions of Si nanowire. $F_s$ is fracture force, $\sigma_f$ is fracture strength and $A_s$ is cross-sectional area of Si nanowire.

$$F_s = \sigma_f A_s \tag{2.4}$$

Spring constant of the Si nanowire ($K_s$) is calculated with Equation (2.5). As shown in Figure (1.1), in order to calculate total spring constant of whole mechanism, spring constant of Si nanowire is needed. Total system spring constant will be used to calculate required electrostatic force needed to fracture the sample.

$$k_s = \frac{A_s E}{l} \tag{2.5}$$

In Figure (1.2), difference of $x_{ACmax}$ with $x_{FSmax}$ is the elongation of sample ($\Delta l$). $x_{AC}$ is the displacement exerted in actuator springs and $x_{FSmax}$ is the total sensor displacement which will be discussed in Chapter 3.

$$\Delta l = \frac{F_s}{k_s} \tag{2.6}$$

From this point all the calculations are completed inside *for loop*s (see Appendix A). For one of each geometrical parameter; comb finger width ($w_{AC}$), comb finger length ($l_{AC}$), $g_x$, $g_y$, overlap (h) and voltage difference (V) calculations are completed and each set of resultant geometry is checked inside the control mechanism.

Actuator design comes after designing the sensor part. Total sensor displacement ($x_{FSmax}$) is needed to calculate total actuator movement and it is calculated with Equation (3.8) in Chapter 3 by using equivalent sensor stiffness. Having calculated $x_{FSmax}$, total actuator displacement is found in Equation (2.7).

$$x_{ACmax} = \Delta l + x_{FSmax} \tag{2.7}$$

$$K_{eq} = \frac{(k_{FS}k_s + k_{AC}k_s + k_{FS}k_{AC})}{(k_{FS}+k_s)} \tag{2.8}$$

To find the electrostatic force ($F_{es}$) in Equation (2.9), second required parameter is the equivalent spring constant of whole system shown in Figure (1.1) and it is calculated in Equation (2.8).

$$F_{es} = x_{ACmax}k_{eq} \tag{2.9}$$

$$N_{AC} = \frac{F_{es}}{\left[\varepsilon_0 t\left(\frac{w_{AC}}{(g_x - x_{ACmax})^2} + \frac{1}{g_y}\right)V^2\right]} \tag{2.10}$$

In Equation (2.10) number of fingers to be used in design is calculated. This number indicates how many pairs of comb finger shown in Figure (2.1) will be used. This number is important for fabrication and it will be discussed in *2.2.2.1. Device Simplicity*.

### 2.2.2. Design Criteria

All equations above give a corresponding output in a specific *for loop*. However, some criteria are needed to filter these results. These criteria are listed as *Device Simplicity*, *Device Stability and Device Linearity*.

#### 2.2.2.1. Device Simplicity

Increasing the amount of comb fingers makes the device more complex. This situation might lead to increase in fabrication failures. As a result of failures, there might be malfunctioning or even not working devices. Therefore, keeping the number of fingers low will handle such problems.

#### 2.2.2.2. Device Stability

Since device simply works with electrostatic principles, pull-in phenomenon is a common problem to handle with. We investigate this phenomenon in two items: horizontal pull-in and vertical pull-in.

One can see that a pair of comb finger structure is symmetrical. However, the main problem is fabrication simply will not be symmetrical. There will always be slight differences between the desired dimensions and fabricated dimensions. In Figure (2.3) schematic A, comb finger moves in horizontal direction. Pull-in distance and voltage should be considered in this manner.

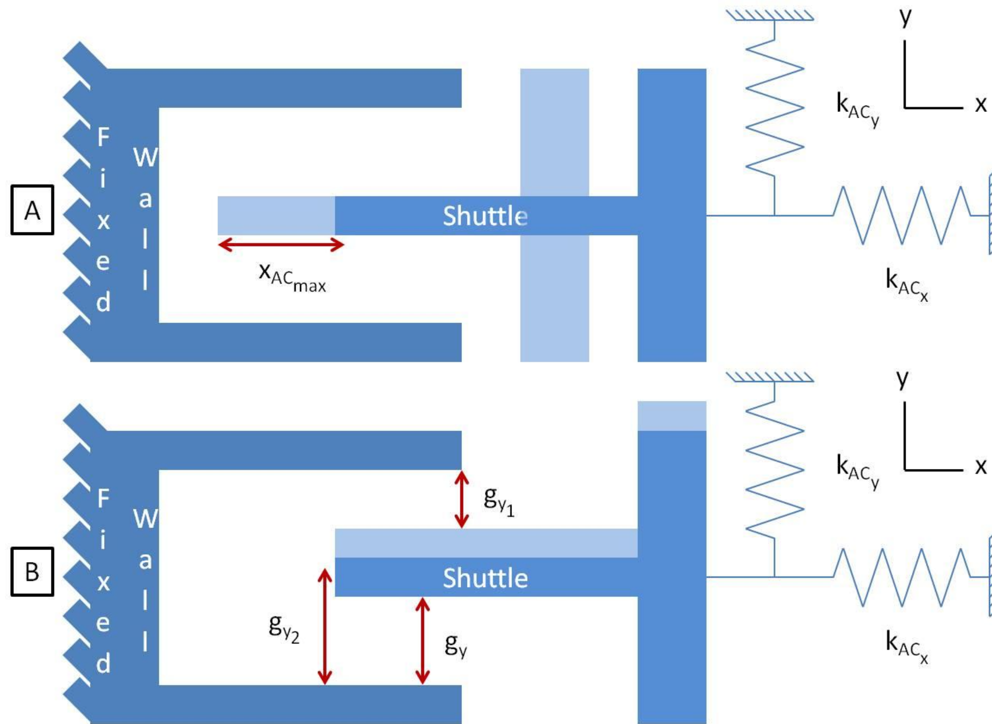


**Figure 2.3**: A: Horizontal displacement of movable fingers, B: Vertical displacement of movable fingers

For horizontal pull-in analysis, there appear two specific conditions. They are given in Equation (2.11) and Equation (2.12). Combining these equations will result with an estimated pull-in distance ($x_{pull\text{-}inx}$) and with Equation (2.13) pull-in voltage ($V_{pull\text{-}inx}$) can be found. To set the filter, $x_{ACmax}$ must not be greater than $x_{pull\text{-}inx}$ and the corresponding voltage difference (V) must not be greater than $V_{pull\text{-}inx}$. If these values simply become greater, device will fail and pull-in will occur.

$$F_{es} = F_{mech} \tag{2.11}$$

$$\frac{\partial F_{es}}{\partial x} = \frac{\partial F_{mech}}{\partial x} \tag{2.12}$$

$$V_{pull-in_x} = \sqrt{x_{pull-in_x} \frac{k_{eq}}{\varepsilon_0 N_{AC} t \left( \frac{w_{AC}}{\left(g_x - x_{pull-in_x}\right)^2} + \frac{1}{g_y} \right)}} \tag{2.13}$$

For vertical pull-in analysis, finding the vertical pull-in voltage ($V_{pull\text{-}iny}$), which is Equation (2.14), is enough to control the parameters. V, applied voltage, value should not exceed $V_{pull\text{-}iny}$ to have a safe design. $k_{ACy}$ indicates the actuator equivalent spring constant in vertical direction. For horizontal pull-in analysis, equivalent spring constant of whole device is used whereas for vertical pull-in analysis we used vertical spring constant of only actuator. The reason behind this situation is that the system as a complete structure (Figure 1.1) behaves much more rigid in horizontal direction than vertical direction.

$$V_{pull-in_y} = \sqrt{\frac{k_{AC_y} {g_y}^3}{2 N_{AC} \varepsilon_0 t (x_{ACmax} + h)}} \tag{2.14}$$

**2.2.2.3 Device Linearity**

Actuator works with two different capacitance generation as shown in Figure (2.1) and Equation (2.2). It is desired that rather than being a parallel plate capacitor, it should be a sliding mechanism. Therefore, we set a ratio for $C_y/C_x$. $C_y$ and $C_x$ are demonstrated in Figure (2.2) respectively. If below relation (2.15) is satisfied, we claim that actuator behaves as a slider mechanism.

$$\frac{C_y}{C_x} = \frac{(h + x_{ACmax})}{g_y} \frac{(g_x - x_{ACmax})}{w_{AC}} > 40 \quad (2.15)$$

## 2.3. Design Output Parameters

**Table 2.1:** First generation actuator design parameters for four different Si nanowires

| Samples | $w_{AC}$ [μm] | h [μm] | $g_x$ [μm] | $g_y$ [μm] | $k_{AC}$ [N/m] | Applied Voltage [V] | $N_{AC}$ | ΔC (fF) |
|---|---|---|---|---|---|---|---|---|
| Nw 1 | 5 | 5 | 155 | 4 | 10 | 40 | 83 | 1.08 |
| Nw 2 | 5 | 5 | 150 | 4 | 11 | 40 | 231 | 7.62 |
| Nw 3 | 5 | 5 | 145 | 4 | 4 | 40 | 337 | 44.60 |
| Nw 4 | 5 | 5 | 145 | 4 | 4 | 40 | 881 | 304.86 |

Table 2.1 shows the first generation actuator geometry parameters. These devices are fabricated and characterization for some of them is completed. However, due to the existence of MOS capacitance which is observed during characterization experiments, new generation device geometry is needed. Considering the MOS effect on the experiments (see Chapter 4 and 5), new design parameters are found as in Table 2.2.

**Table 2.2:** New generation actuator design parameters for four different Si nanowires

| Samples | $w_{AC}$ [μm] | h [μm] | $g_y$ [μm] | $g_x$ [μm] | $k_{AC}$ [N/m] | Applied Voltage [V] | $N_{AC}$ | ΔC (fF) |
|---|---|---|---|---|---|---|---|---|
| Nw 1 | 5 | 70 | 2 | 10 | 10.41 | 10 | 658 | 19.90 |
| Nw 2 | 5 | 70 | 2 | 10 | 11.44 | 15 | 756 | 54.45 |
| Nw 3 | 5 | 70 | 2 | 10 | 4.04 | 20 | 618 | 208.52 |
| Nw 4 | 5 | 70 | 2 | 10 | 4.50 | 25 | 1023 | 776,99 |

New actuator design parameters for four different Si nanowires are found for 10 μm device layer and 2 μm BOX layer thickness. Previously, usage of 1 μm BOX layer resulted with a dominating MOS capacitance effect. Comparing the new and old designs, there are some significant varieties. Overlap (h) is quite higher in new design to increase the initial capacitance value for MEMS. This will provide compatibility for MEMS and MOS capacitances. In addition, dominancy for capacitance change is another expectation from new design parameters. Revisiting Equation (2.3), it is the applied voltage difference value that directly affects the capacitance change so that we intentionally lowered voltage values while having the force value fixed. Along this insight, checking the capacitance difference values ($\Delta C$), which are the difference capacitance values of 0 voltage capacitance and finally applied voltage capacitance, of both new and old designs, a significant increase in MEMS capacitance is observable. This will enable more readability range for characterization. Since the least capacitance difference value is of nanowire 1 actuator, most probably, characterization steps will be the hardest among other actuators. Since nanowire 1 is the smallest in dimension, we expect such challenges for our design.

# Chapter 3

# FORCE SENSOR MODELLING AND DESIGN

## 3.1. System Overview

Sensor designed throughout this project is the source of displacement and force detection. Working principle of the mechanism relies on the differential capacitance between three parallel plates. As Figure 3.1 shows, two of the plates are fixed and other one is the moving shuttle. Fixed plates are exited with AC voltage having 180° phase difference while moving part remains still. Displacement generated by actuator is shared between Si nanowire spacemen and the force sensor so that the changing gap between fixed and moving sensor comb fingers causes capacitive difference. Finally, capacitance difference generates a voltage output on the shuttle. In this project, Si is used as the fabrication material. Since Si is semi-conductor, to measure the output voltage on the moving shuttle, whole device will be coated with a conductor material, Au.

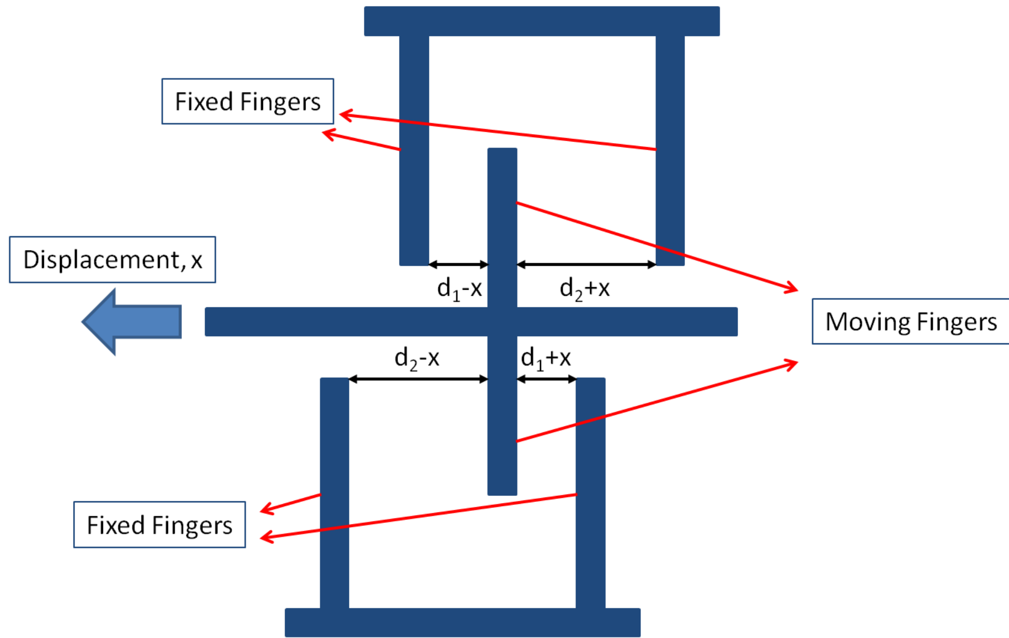


**Figure 3.1**: Force sensor schematic

Since differential capacitance has the utmost importance, one can write the overall capacitance difference as in Equation (3.4).

$$C_1 = N_{FS}\varepsilon_0 t l_{FS}\left(\frac{1}{d_1 - x} + \frac{1}{d_2 + x}\right) \tag{3.1}$$

$$C_2 = N_{FS}\varepsilon_0 t l_{FS}\left(\frac{1}{d_1 + x} + \frac{1}{d_2 - x}\right) \tag{3.2}$$

$$\Delta C = C_1 - C_2 \tag{3.3}$$

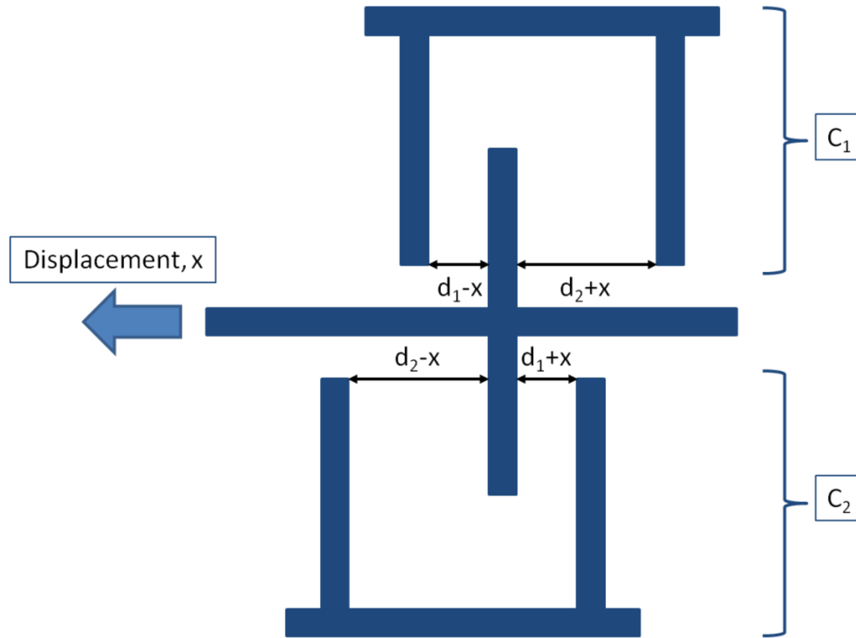


**Figure 3.2**: Capacitances on force sensor. $C_1$ is total capacitance value of upper comb fingers; $C_2$ is total capacitance value of lower comb fingers.

$$\Delta C = 2N_{FS}\varepsilon_0 t l_{FS} x \left(\frac{1}{d_1^2 - x^2} - \frac{1}{d_2^2 - x^2}\right) \tag{3.4}$$

In above equation, ΔC is the capacitance difference between fixed and moving comb fingers shown in Figure 3.2. $\varepsilon_0$ is relative permittivity of air, $N_{FS}$ is the finger amount of the force sensor and t is the thickness of the device.

Applying AC signal having 180° phase angle to the fixed walls, capacitive difference can be converted to AC signal on the moving shuttle as $V_{readout}$ (Equation (3.5)).

$$V_{readout} = aV_{FS}\Delta C = 2aN_{FS}\varepsilon_0 t l_{FS} V_{FS} \left(\frac{1}{d_1^2 - x^2} - \frac{1}{d_2^2 - x^2}\right) x \tag{3.5}$$

In Equation (3.5), $V_{FS}$ is the excitation voltage on the fixed walls, *a* is a constant that is related with the interfacial dynamics and this value is set to $\frac{1}{C_{tot}}$ [22]. $C_{tot}$ is the total capacitance of the system which will be mentioned later.

### 3.2. Design Algorithm

In this project, sensor design is carried out with an algorithm as outlined in Figure 3.3. We reach the final geometry values by applying specific formulas, which are explained in later subtitles, for the sample and wafer material specifications.

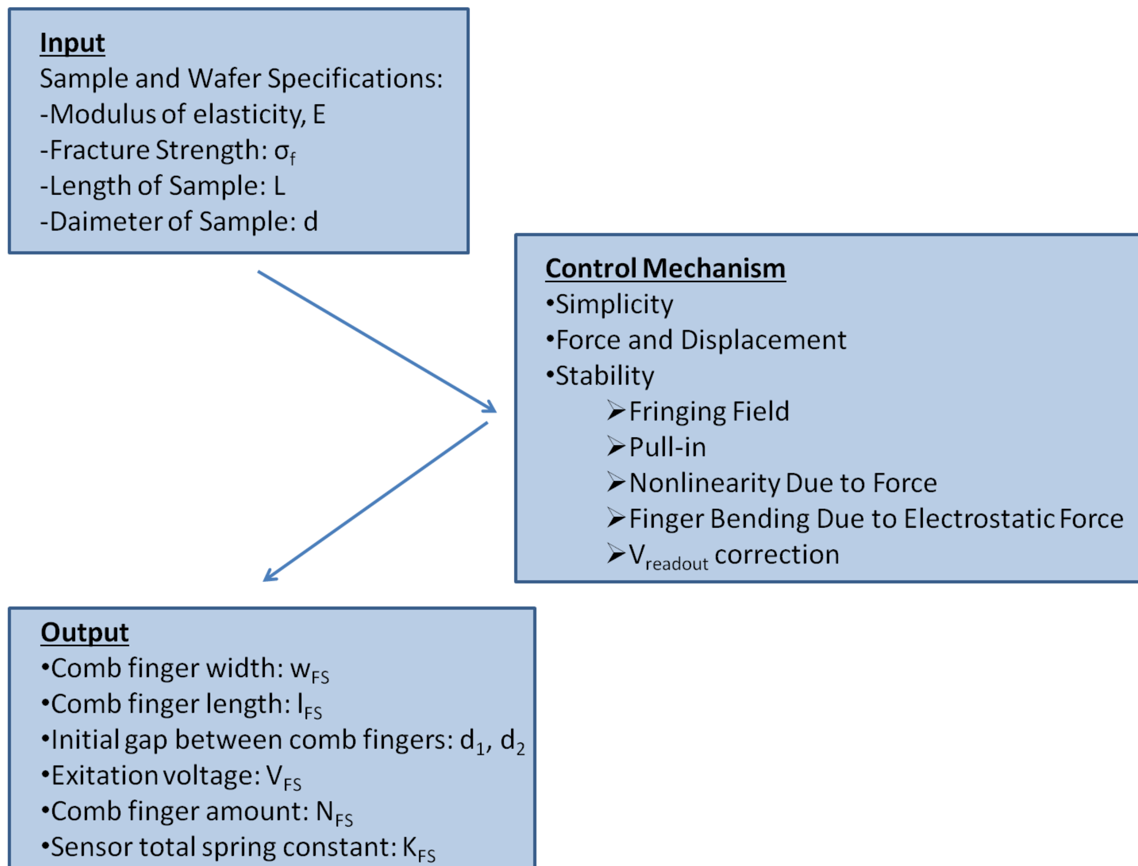


**Figure 3.3**: Force sensor design algorithm

### 3.2.1. Formulations

Design parameters are found via a MATLAB code having below formulas. Si material specifications (modulus of elasticity and fracture strength), desired Si nanowire dimensions (length and diameter), device layer thickness of SOI (Silicon-on-insulator) wafer are encoded at once.

Using Equation (3.6), force required for fracture of Si nanowire is calculated due to a desired geometry of Si nanowire. $F_s$ is fracture force, $\sigma_f$ is fracture strength and "A" is cross-sectional area of Si nanowire.

$$F_s = \sigma_f A \tag{3.6}$$

Considering the mass-spring model of whole MEMS device including an actuator, a specimen and a sensor, Si specimen and sensor are serially connected. As a result of serial connection, the force on each item is same. For later formulas, Equation (3.7) is used. $F_{FS}$ notates the force on sensor.

$$F_s = F_{FS} \tag{3.7}$$

From this point all the calculations are completed inside *for loop*s (see Appendix A). For one of each geometrical parameter; comb finger width ($w_{FS}$), comb finger length ($l_{FS}$), data amount ($N_{data}$), $d_1$, $d_2$, and excitation voltage ($V_{FS}$) calculations are completed and each set of resultant geometry is checked inside the control mechanism.

Since the complexity of the calculations and formulas, "x" parameter shown in Figure 3.1 and Figure 3.2 will be stated as $x_{FS}$ inside the formulas. First calculation inside the "for loops" is to find total displacement of the sensor until Si nanowire fractures ($x_{FSmax}$) (Equation (3.8)). The ratio of this value to $d_1$ is used as a parametric value for

linearity check calculations (Equation (3.9)). Since there is a specific amount of data points which is planned to be gathered, the displacement value for each data point is also needed to be calculated (Equation (3.10)).

$$x_{FSmax} = \frac{F_{FS}}{k_{FS}} \tag{3.8}$$

$$\tilde{x}_{max} = \frac{x_{FSmax}}{d_1} \tag{3.9}$$

$$x_{FSstep} = \frac{x_{FSmax}}{N_{data}} \tag{3.10}$$

Next step is to calculate number of comb fingers by using Equation (3.11). In this formula, $\Delta C_{min}$ represents the minimum capacitance value that the semi-conductor parameter analyzer can measure. Nevertheless, formula gives the corresponding number of comb fingers to have $\Delta C_{min}$ capacitance value for a displacement value of $x_{FSstep}$. Number of fingers ($N_{FS}$) is going to be used for determining the overall capacitance difference.

$$N_{FS} = \frac{\Delta C_{min}}{\frac{1}{d_1^2 - x_{FSstep}^2} - \frac{1}{d_2^2 - x_{FSstep}^2}} \frac{1}{2\varepsilon_0 t l_{FS} x_{FSstep}} \tag{3.11}$$

Stability analysis of sensor is complex due to having tri-plate differential capacitance mechanism. As for the actuator, simply calculating the pull-in voltage and pull-in distance does not work for sensor. However, one should mark the importance of electrostatic force between the moving and fixed comb fingers. Moving comb fingers will bend due to the electrostatic force (Equation (3.12)) as in Figure 3.4 so that bending should not be problematic for displacement of whole shuttle. It is expected that the dominant factor for capacitance generation should be nanowire elongation rather than finger bending.

$$F_{es_FS} = 2N_{FS}\varepsilon_0 t l_{FS} x_{FS} {V_{FS}}^2 \left( \frac{d_1}{(d_1^2 - x_{FS}^2)^2} + \frac{d_2}{(d_2^2 - x_{FS}^2)^2} \right) \quad (3.12)$$

$$F_{mech} = k_{FS} x_{FS} \quad (3.13)$$

$$x_{bending} = \frac{3{l_{FS}}^3 \varepsilon_0 {V_{FS}}^2}{k_{FS}} \left( \frac{d_1}{\left({d_1}^2 - {x_{FSmax}}^2\right)^2} + \frac{d_2}{\left({d_2}^2 - {x_{FSmax}}^2\right)^2} \right) \frac{x_{FSmax}}{E{w_{FS}}^3} \quad (3.14)$$

In the formulas, $F_{mech}$ is the mechanical balancing force, $k_{FS}$ is the total spring constant of sensor, $x_{FS}$ is the shuttle displacement in any time during shuttle movement, *E* is modulus of elasticity of Si, *w* is width of comb finger.

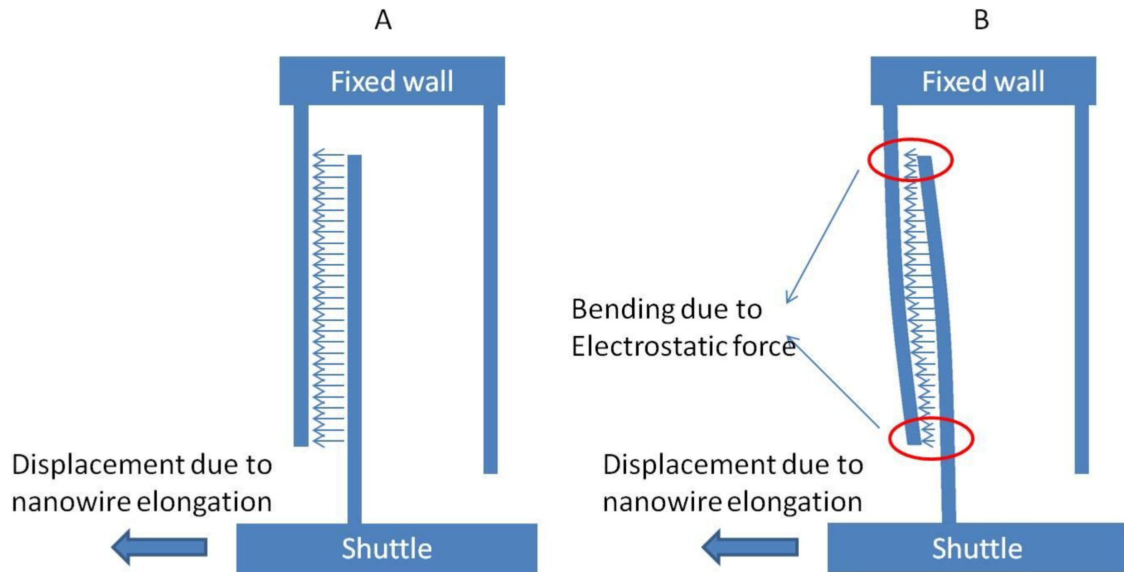


**Figure 3.4**: Finger bending due to electrostatic force. Part A shows the initial position of a finger pair for the upper part of sensor. Part B shows the finger positions due to nanowire displacement and electrostatic force.

As previously stated, pull-in calculation for tri-plate mechanism is complex so that in order to have insight about the working limits of sensor, some approximations are made. δ is set to be the ratio of electrostatic force to balancing mechanical force ($F_{mech}$). $F_t$=ma is external force, b is the ratio of $d_2$ to $d_1$ and $\tilde{x}$ is the ratio of $x_{FS}$ to $d_1$. Considering the new variables, formulas can be rewritten as following:

$$\delta = \frac{2{V_{FS}}^2 N_{FS}\varepsilon_0 A}{k_{FS} d_1^3} \tag{3.15}$$

$$\frac{F_t}{k_{FS} d_1} = \tilde{x}\left(1 - \delta\left[\frac{1}{b^3\left(1-\frac{\tilde{x}^2}{b^2}\right)^2} + \frac{1}{(1-\tilde{x}^2)^2}\right]\right) \tag{3.16}$$

Thinking $\frac{F_t}{k_{FS} d_1}$ as a function and plotting the graph or solving it analytically, critical points for displacement can be found. Sensor's nonlinearity due to force (citation=Zhang) (Equation (3.17)) is another parameter to be considered and it will be discussed in 2.2.2. Control Criteria.

$$NL_F(\tilde{x}) = \frac{\tilde{x}}{\tilde{x}_{max}}\left\{\frac{\left(\frac{1}{1-\tilde{x}^2} - \frac{1}{b^2-\tilde{x}^2}\right)}{\left(\frac{1}{1-{\tilde{x}_{max}}^2} - \frac{1}{b^2-{\tilde{x}_{max}}^2}\right)} - \frac{\left[1-\delta\left(\frac{b}{(b^2-\tilde{x}^2)^2} + \frac{1}{(1-\tilde{x}^2)^2}\right)\right]}{\left[1-\delta\left(\frac{b}{\left(b^2-{\tilde{x}_{max}}^2\right)^2} + \frac{1}{\left(1-{\tilde{x}_{max}}^2\right)^2}\right)\right]}\right\} \tag{3.17}$$

As the last step, total capacitance of the sensor (Equation (3.18)) and sensitivity due to displacement (Equation (3.19)) is calculated with the following formulas. In Equation

(3.19) $k_s$ is the sample spring constant, which is Si nanowire in our case and $l_s$ is the length of the sample.

$$C_{tot} = 2N_{FS}\varepsilon_0 l_{FS} t\left(\frac{1}{d_1} + \frac{1}{d_2}\right) \tag{3.18}$$

$$S = \frac{V_{readout}}{\frac{x_{FSmax}k_{FS}}{k_s l_s}} \tag{3.19}$$

### 3.2.2. Design Criteria

All equations above give a corresponding output in a specific *for loop*. However, some criteria are needed to filter these results. These criteria are listed as *Force and Displacement Data for Fracture*, *Device Simplicity*, *Device Stability and Nonlinearity of Measurement*.

#### 3.2.2.1 Force and Displacement Data for Fracture

Sample dimensions are highly effective in determination of sensor displacement and fracture force. Fracture strength values are specific for each material. However, fracture force might be different due to cross-sectional area of the sample. Moreover, elongation until fracture might vary because of length difference. Therefore, thinking on specific sample dimensions helps determining the correct geometric parameters such as finger amount, width, length etc.

#### 3.2.2.2. Device Simplicity

Increasing the amount of comb fingers makes the device more complex. This situation might lead to increase in fabrication failures. As a result of failures, there might be malfunctioning or even not working devices. Therefore, keeping the number of fingers low

will handle such problems. Generally, setting the finger amount 1000 as a maximum limit for filtering is a good option. If one will design too small samples having $10^4$ $nm^3$ or smaller volumes number can be increased to 5000. Fabrication will be more problematic and in addition springs of the sensor should be designed for carrying all the weight.

#### 3.2.2.3. Device Stability

Design parameters taken from the code should also undergo a stability check in five subtitles listed as *Fringing Field*, *Pull-in*, *Nonlinearity Due to Force*, *Finger Bending Due to Electrostatic Force* and *Readout Voltage Correction*.

##### 3.2.2.3.1. Fringing Field

$\tilde{x}_{max}$ value which is calculated in Equation (3.9) should not exceed 0.5 (citation).

##### 3.2.2.3.2. Pull-in

Device working principle fundamentally stands on differential capacitive reading which is directly related with electrostatics. Pull-in is a common problem for electrostatically actuated comb fingers. In our case, as previously mentioned formula approximations state; considering the result of Equation (3.16) as series, maximum element of that should not exceed $\tilde{x}_{max}$ value.

##### 3.2.2.3.3. Nonlinearity due to Force

±%5 is set to be the limiting range for nonlinearity of sensor. Within these limits sensor is considered as linear. Equation (3.17) is used to check the nonlinearity percentage.

#### 3.2.2.3.4. Finger Bending Due to Electrostatic Force

In Equation (3.14) finger bending is already calculated. considering 2.2.2.3.1. Fringing Field analysis, maximum working distance is $d_1/2$. Therefore, finger bending should be smaller than the difference of $d_1/2$ with $x_{FSmax}$.

#### 3.2.2.3.5. Readout Voltage Correction

Readout voltage ($V_{readout}$) is calculated with Equation (3.5). This value should exceed the multiplication of $V_{out_min}$ and $N_{data}$. $V_{out_min}$ is the minimum readable voltage value for a specific semiconductor parameter analyzer.

## 3.3. Designed Sensor Parameters

**Table 3.1:** First generation sensor design parameters for four different Si nanowires

| Samples | $w_{FS}$ [μm] | $l_{FS}$ [μm] | $d_1$ [μm] | $d_2$ [μm] | $k_{FS}$ [N/m] | Applied Voltage [$V_{FS}$] | Sensitivity [V/(μm/μm)] | $N_{FS}$ |
|---|---|---|---|---|---|---|---|---|
| Nw 1 | 8 | 800 | 5 | 45 | 3 | 2 | 1.53 | 590 |
| Nw 2 | 8 | 750 | 5 | 40 | 3 | 2 | 6.66 | 153 |
| Nw 3 | 8 | 770 | 6 | 30 | 6 | 2 | 6.57 | 171 |
| Nw 4 | 8 | 750 | 5 | 30 | 20 | 2 | 7.34 | 136 |

The design data in Table 3.1 could not be fabricated properly. Reasons and suggestion for next generation will be discussed in detail in Chapter 4. However, in order not to encounter same MOS capacitance effect for force sensor characterization, we redesigned by considering the following derivations.

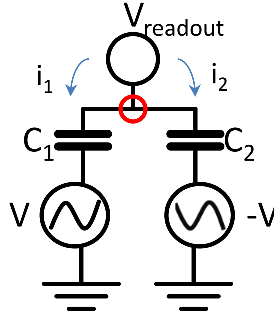


**Figure 3.5:** Lump model of force sensor having no MOS effect. $i_1$ and $i_2$ are the currents coming out of red node.

$$i_1 + i_2 = \frac{V_{readout} - V}{\frac{1}{jwC_1}} + \frac{V_{readout} - (-V)}{\frac{1}{jwC_2}} = 0$$

$$(V_{readout} - V)jwC_1 + (V_{readout} + V)jwC_2 = 0$$

$$(V_{readout} - V)C_1 + (V_{readout} + V)C_2 = 0$$

$$V_{readout}(C_1 + C_2) + V(C_2 - C_1) = 0$$

$$V_{readout}(C_1 + C_2) = V(C_1 - C_2)$$

$$V_{readout} = \frac{V(C_1 - C_2)}{C_1 + C_2} = \frac{V\Delta C}{C_{tot}} \tag{3.20}$$

Equation (3.20) has the same result with Equation (3.5) which means our lump model implementation is correct so that we introduce additional MOS capacitance effect into the system and we get the configuration in Figure (3.6) and the following derivation.

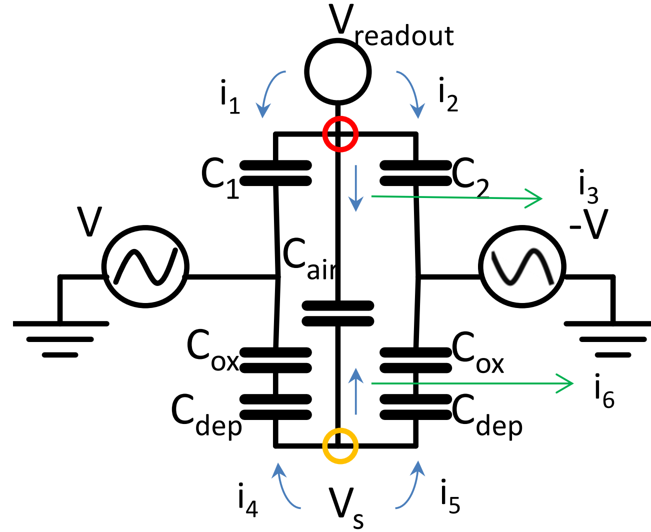


**Figure 3.6**: Lump model of force sensor including MOS effect. $V_s$ is the handle layer voltage, $i_1$, $i_2$ and $i_3$ are the currents coming out of red node, $i_4$, $i_5$ and $i_6$ are the currents coming out of orange node.

$$i_1 + i_2 + i_3 = \frac{V_{readout} - V}{\frac{1}{jwC_1}} + \frac{V_{readout} - (-V)}{\frac{1}{jwC_2}} + \frac{V_{readout} - V_s}{\frac{1}{jwC_{air}}} = 0$$

$$(V_{readout} - V)jwC_1 + (V_{readout} + V)jwC_2 + (V_{readout} - V_s)jwC_{air} = 0$$

$$(V_{readout} - V)C_1 + (V_{readout} + V)C_2 + (V_{readout} - V_s)C_{air} = 0$$

$$V_{readout}(C_1 + C_2 + C_{air}) + V(C_2 - C_1) - V_s C_{air} = 0 \tag{3.21}$$

$$C_{eq} = \frac{C_{ox} C_{dep}}{C_{ox} + C_{dep}}$$

$$i_4 + i_5 + i_6 = \frac{V_s - V}{\frac{1}{jwC_{eq}}} + \frac{V_s - (-V)}{\frac{1}{jwC_{eq}}} + \frac{V_s - V_{readout}}{\frac{1}{jwC_{air}}} = 0$$

$$(V_s - V)jwC_{eq} + (V_s + V)jwC_{eq} + (V_s - V_{readout})jwC_{air} = 0$$

$$(V_s - V)C_{eq} + (V_s + V)C_{eq} + (V_s - V_{readout})C_{air} = 0$$

$$V_s(2C_{eq} + C_{air}) - V_{readout}C_{air} = 0$$

$$V_s(2C_{eq} + C_{air}) = V_{readout}C_{air}$$

$$V_s = \frac{V_{readout}C_{air}}{(2C_{eq}+C_{air})}$$

Placing $V_s$ into Equation (3.21), we get

$$V_{readout}(C_1 + C_2 + C_{air}) + V(C_2 - C_1) - \frac{V_{readout}C_{air}}{(2C_{eq}+C_{air})}C_{air} = 0$$

$$V_{readout}\left(C_1 + C_2 + C_{air} - \frac{{C_{air}}^2}{(2C_{eq}+C_{air})}\right) + V(C_2 - C_1) = 0$$

$$V_{readout}\left(C_1 + C_2 + C_{air} - \frac{{C_{air}}^2}{(2C_{eq}+C_{air})}\right) = V(C_1 - C_2)$$

$$V_{readout} = \frac{V(C_1 - C_2)}{\left(C_1 + C_2 + C_{air} - \frac{{C_{air}}^2}{(2C_{eq} + C_{air})}\right)} \quad (3.22)$$

**Table 3.2:** New generation sensor design parameters for four different Si nanowires

| Samples | $w_{FS}$ [µm] | $l_{FS}$ [µm] | $d_1$ [µm] | $d_2$ [µm] | $k_{FS}$ [N/m] | Applied Voltage [$V_{FS}$] | Sensitivity [V/(µm/µm)] | $N_{FS}$ |
|---|---|---|---|---|---|---|---|---|
| Nw 1 | 5 | 200 | 4.5 | 23.75 | 4.5 | 2 | 0.65 | 3169 |
| Nw 2 | 5 | 200 | 2.25 | 11.25 | 10 | 2 | 3.26 | 395 |
| Nw 3 | 5 | 200 | 2 | 10 | 18 | 2 | 5.46 | 220 |
| Nw 4 | 5 | 200 | 2 | 10 | 76 | 2 | 3.74 | 314 |

Table 3.2 is generated by using Equation (3.22) as the final voltage readout. Considering the number of fingers in Table 3.2, finger amount of force sensor of $1^{st}$ nanowire is quite higher. Since the expected elongation value is so small, to detect the deformation of nanowire, such force sensor is needed.

# Chapter 4

# FABRICATION

## 4.1 Introduction

Si test wafer fabrication characterizations (for SEM images, see Appendix B) and device fabrications are carried out in Center of MicroNano Technology (CMi), EPFL.

## 4.2 Chrome Mask Fabrication

A corresponding chrome mask needs to be prepared before device fabrication. In general, aim is to transfer the device geometries and wafer level arrangement onto the glass plate drawn via a commercial software environment L-Edit. In later steps of device fabrication, chrome masks are used for photolithography to print the masks onto the photoresist. The originally purchased glass mask plate comes with a 5" glass plate having Chrome and photoresist on it. As the first step, having the photoresist side on top, glass plate is placed inside DWL 200 Heidelberg laser mask writer. DWL 200 Heidelberg starts printing the corresponding mask drawings after finishing the required arrangements in the device specific software. During the printing, laser makes the photoresist chemically change its structure in specific areas.

Before placing glass plate in Suess DV10 Photoresist Developer, device should be purged. Completing the purge, glass plate is placed in the device. Development step is

carried out with "Cr Blank 5P Fine" option. In development step, corresponding areas of photoresist are removed to create areas for chrome etching.

Chrome etch is carried out in wet bench. Glass plate is kept in a solution for 90 seconds by using a Teflon holder. The solution etches the printed chrome areas. Completing chrome etch, glass plate is washed for 3-4 minutes and dried via Nitrogen gun. Chrome mask on the glass plate is ready to be used in later steps of fabrication. In this project, one chrome mask is fabricated for actuator device layer etch while two chrome masks are fabricated for force sensor device layer and handle layer.

## 4.3. Actuator Fabrication

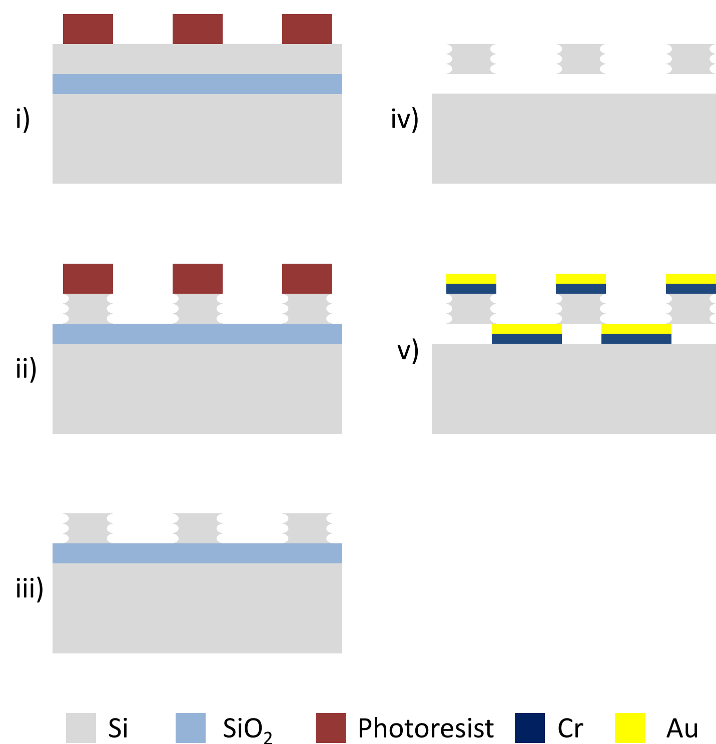


**Figure 4.1:** Fabrication process flow for actuator. i) Photoresist coating, photolithography and development, ii) BOSCH process, iii) Photoresist strip and scribing, iv) HF vapor release, v) E-beam evaporation.

### 4.3.1. HMDS and Photoresist Coating

First generation fabrication is carried out with 4" SOI (Silicon-on-Insulator) wafer. SOI wafer used for this project consists of 10 µm silicon device layer, 1 µm BOX (Buried Oxide) and 380 µm silicon handle layer. First step for fabrication is the wafer preparation with HMDS. After 23-minute HMDS, to coat SOI device layer with AZ92xx negative photoresist, device is placed in EVG 150 Coater and Developer. 5 µm of AZ92xx negative photoresist is coated for 15 minutes (Figure 4.1.i).

Completing the coating, 8 minutes of relaxation time for photoresist is required and wafer is checked for not having small bubbles. If those bubbles exist on the photoresist coating, during the photolithography step those areas will not be printed and most probably in the next steps of fabrication will result with a malfunctioning structure.

### 4.3.2. Photolithography

Photolithography is the printing step of formerly fabricated chrome mask onto the photoresist coated SOI wafer. Süss MA6/BA6 Double Sided Mask Aligner is used for photolithography. SOI wafer is exposed to UV light for 17.5 seconds with "hard contact" option. "Hard contact" is used to have better resolution while printing (Figure 4.1.i).

### 4.3.3. Development

To complete the printing, development step should be finished as soon as possible after photolithography. Since AZ92xx negative photoresist is used for coating, during the photolithography chemically changed areas of photoresist form the mask for later use and remaining chemically not-changed parts should be removed. During development, these parts are removed and the complete photoresist mask is generated. This step is carried out in EVG 150 by using a suitable recipe (Figure 4.1.i).

### 4.3.4. SRD (Spin-Rinse-Dryer) & Device Layer Si Etch

It is strongly recommended that right after the development, SOI wafer should be cleaned before Si etch. Previous steps might contaminate the wafer with undesired particles due to the usage of different machines and stages. To evade them, 7-10 minutes of cleaning and drying is carried out with SRD machine.

To etch device layer Si, "SOI accurate ++" recipe is used in Alcatel AMS 200 DSE. With this recipe 10 μm Si is etched for 3 minutes and 8 seconds (BOSCH Process). Time required to etch Si can be changed due to the weekly calibration of the machine. After 10 μm device layer Si etching, fabricated device appears (Figure 4.1.ii).

### 4.3.5 Photoresist Removal & Scribing

After device layer Si etch, remaining photoresist on the device layer which served as mask during etching is removed by using oxygen plasma in Tepla GiBAbatch for 15-20 minutes (Figure 4.1.iii). Following the removal of the photoresist, wafer is scribed into chips for further steps of BOX removal and Cr-Au coating.

### 4.3.6. BOX Removal

BOX is the only layer between the device layer and handle layer. After device layer Si etching, to release the fabricated device, BOX is removed via HF vapor (Figure 4.1.iv). This is a dry process and used to prevent stiction. In case of using a wet process, super critical $CO_2$ drying should be considered otherwise stiction might occur between the comb-fingers. After 3 hours of HF vapor release 1 μm BOX is removed from the open areas. Only the BOX layer under the fixed walls of comb-fingers and spring anchors are not removed during this step.

### 4.3.7 Cr-Au Coating

Figure 4.2 shows the SEM image of an actuator having no Cr-Au coating (see Appendix B for other SEM images). Last step of fabrication is to coat the wafer with chrome and gold (Figure 4.1.v). This step is added to fabrication to be able to do characterization after fabricating the devices. For characterization electrically conductor material is needed for voltage transfer on the wafer, because Si is a semi conductor material. 10 nm Cr is used to make connection between Si and Au because Si and Au cannot merge directly. 300 nm Au is coated onto the 10 nm Cr with e-beam evaporation in Laybold Optics 600H for about 3 hours.

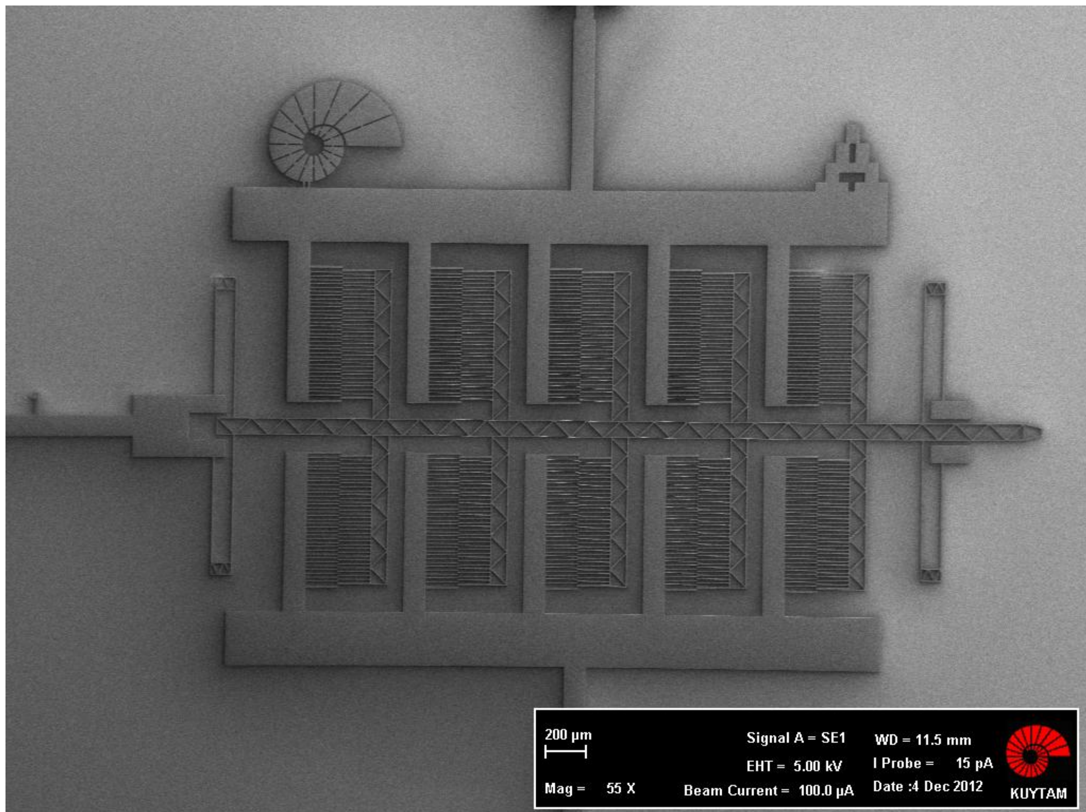


**Figure 4.2:** SEM picture of a fabricated actuator

### 4.4 Force Sensor Fabrication

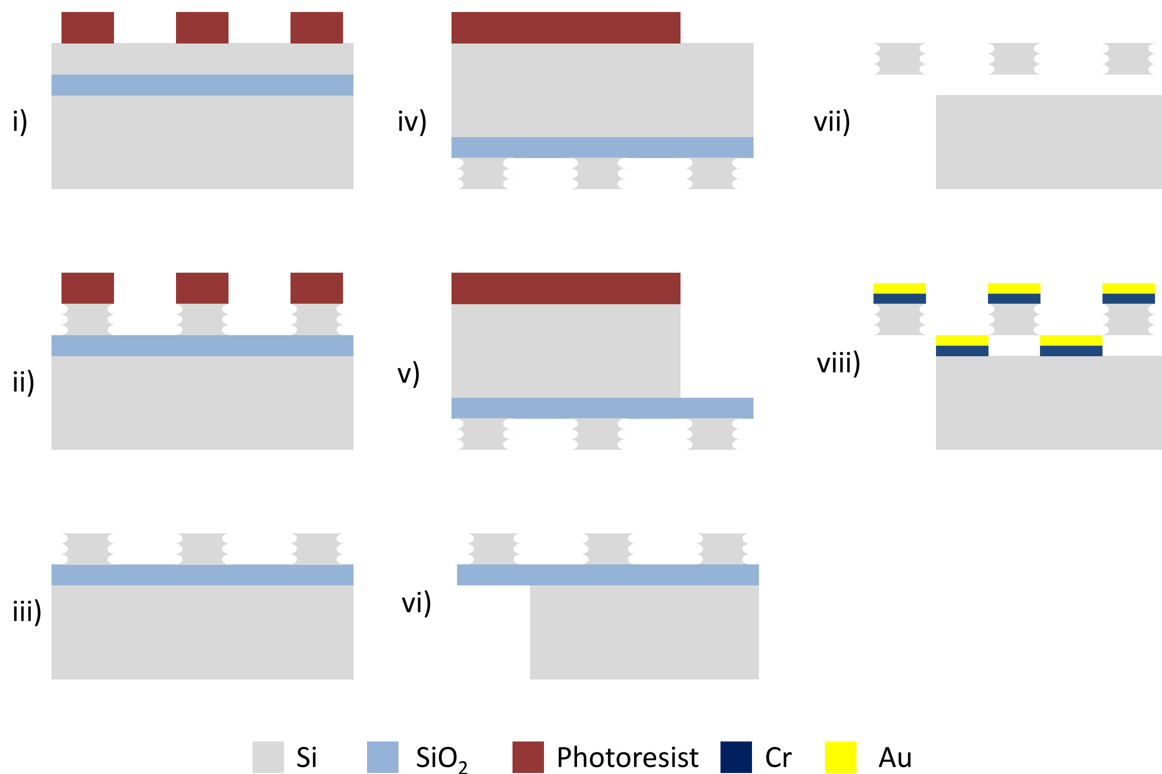


**Figure 4.3:** Fabrication process flow for force sensor. i) Photoresist coating, photolithography and development, ii) BOSCH process, iii) Photoresist strip, iv) Handle layer photoresist coating, photolithography and development, v) Dry etch, vi) Photoresist strip and scribing, vii) HF vapor release, viii) E-beam evaporation.

For the force sensor fabrication, SOI wafer having 10 μm device layer, 1 μm BOX and 380 μm handle layer is used. From 4.4.1 to the end of 4.4.4, force sensor fabrication steps are same with actuator fabrication. Because of having the same quality SOI wafer, time durations for coating, development and etching are same, too. Following subtitle will

begin as 4.4.5 indicating that from 4.4.1 to 4.4.4 the fabrication is same as from 4.3.1 to 4.3.4 and steps will continue with 4.4.5 (Figure 4.3.i-ii-iii).

**4.4.5 Photoresist Strip**

After device layer Si etch, remaining photoresist on the device layer which served as mask during etching is removed by using oxygen plasma in Tepla GiBAbatch for 15-20 minutes (Figure 4.3.iii).

**4.4.6. Handle Layer Photoresist Coating**

Since back side (handle layer) Si will be etched 380 µm, the required resist thickness to act as mask is different than device layer coating thickness. According to the EPFL website, corresponding thickness should be 8 µm for AZ92xx negative photoresist. SOI wafer is placed in EVG 150 and 8 µm AZ92xx is coated with an appropriate recipe (Figure 4.3.iv).

Completing the coating, 15 minutes of relaxation time for photoresist is required and wafer is checked for not having small bubbles. If those bubbles exist on the photoresist coating, during the photolithography step those areas will not be printed and most probably fabrication will result with a failure.

**4.4.7. Handle Layer Photolithography**

Süss MA6/BA6 Double Sided Mask Aligner is used for photolithography. Unlike device layer photolithography step, handle layer is exposed to UV light for 23 seconds with "hard contact" option due to having thicker photoresist coating. "Hard contact" is used to have better resolution while printing (Figure 4.3.iv).

#### 4.4.8. Handle Layer Development

To complete the printing, development step should be finished as soon as possible after photolithography. Since AZ92xx negative photoresist is used for coating, during the photolithography chemically changed areas of photoresist form the mask for later use and remaining chemically not-changed parts should be removed. During development, these parts are removed and the complete photoresist mask is generated. This step is carried out in EVG 150 by using an appropriate developer recipe (Figure 4.3.iv).

#### 4.4.9. SRD (Spin-Rinse-Dryer) & Handle Layer Si Etch

It is strongly recommended that right after the development, SOI wafer should be cleaned before Si etch. Previous steps might bring undesired particles onto the wafer due to the usage of different machines and stages. To evade them, 7-10 minutes of cleaning and drying completed with SRD machine.

To etch device layer Si, "SOI accurate ++" recipe is used in Alcatel AMS 200 DSE. With this recipe we aim to etch 380 µm Si for 120 minutes (BOSCH Process) (Figure 4.3.v). Time required to etch Si can be changed due to the weekly calibration of the machine. After 380 µm handle layer Si etching, underneath the BOX layer it should appear a big-scale gap. Moreover, only 1 µm BOX layer is carrying all the generated intrinsic stress in the wafer so that, while etching is about to end, our SOI wafer failed. Later steps could not be completed due to wafer failure. In order to overcome this problem for next fabrication trial, we introduce an intermediate step. This step goes right between *4.4.5. Photoresist Removal* and *4.4.6. Handle Layer Photoresist Coating*. It is strongly suggested that device layer should be coated with a conformal protective layer which will conserve the rigidity of the SOI wafer during handle layer Si etching. We designated Parylene is an appropriate material that is needed for this purpose. For revised fabrication process flow

schematic, see Figure 7.1. For a full insight about fabrication process flow, remaining steps are explained in the following subtitles.

### 4.4.10. Handle Layer Photoresist Strip & Scribing

After handle layer Si etch, remaining photoresist on the device layer which served as mask during etching should be removed by using oxygen plasma in Tepla GiBAbatch for 15-20 minutes (Figure 4.3.vi). For revised fabrication flow, conformal protective layer should be removed in this step, too. Following the removal of the photoresist and protective layer, wafer is scribed into chips for further steps of BOX removal and Cr-Au coating.

### 4.4.11. BOX Removal

BOX is the only layer between the device layer and handle layer. After device layer Si etching, to release the fabricated device, BOX is removed via HF vapor (Figure 4.3.vii). This is a dry process and used to prevent stiction. In case of using a wet process, super critical $CO_2$ drying should be considered otherwise stiction might occur between the comb-fingers. For actuator, 3 hours of HF vapor release for 1 μm BOX removal is performed. However, since force sensor will have its handle layer Si etched, there will be more open areas for HF vapor to interact with BOX layer, so that less HF vapor application time will introduce a successful BOX removal. Only the BOX layer under the fixed walls of comb-fingers and spring anchors are not removed during this step.

### 4.4.12. Cr & Au Coating

Last step of fabrication, which is same for the actuator, is to coat the wafer with chrome and gold (Figure 4.3.viii). This step is added to fabrication to be able to do characterization after fabricating the devices. For characterization electrically conductor material is needed for voltage transfer on the wafer, because Si is a semi conductor

material. 10 nm Cr is used to make connection between Si and Au because Si and Au cannot merge directly. 300 nm Au is coated onto the 10 nm Cr with e-beam evaporation in Laybold Optics 600H for about 3 hours.

# Chapter 5

# CHARACTERIZATION

## 5.1. Actuator Characterization

### 5.1.1. Setup

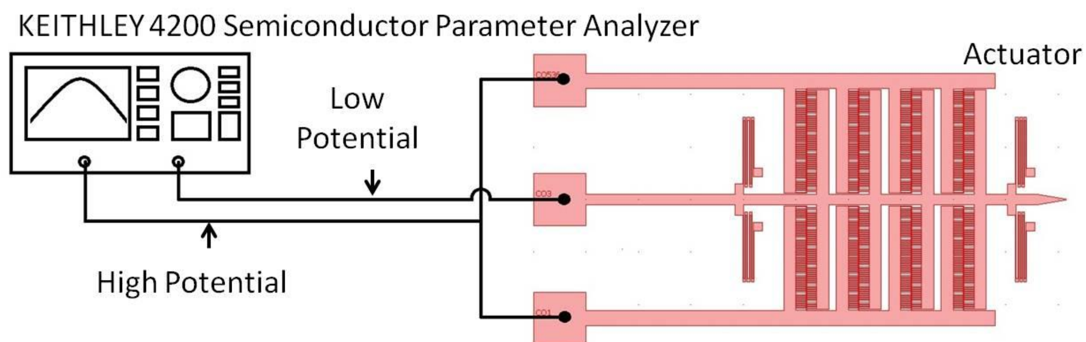


**Figure 5.1:** Capacitance measurement setup for actuator

In order to understand the compatibility of fabricated devices and theoretical calculations, capacitance measurements are required for actuator. Since there is no working device for force sensor, their characterization step is in theory and will be discussed in 5.2. Force Sensor Characterization. Characterization results in this chapter are taken at Micro Nano Characterization Lab. (MNL), Boğaziçi University. Fixed walls of actuator are applied with a voltage value of 30V while setting shuttle at ground. KEITHLEY 4200 has four different ports for this purpose: low current - low potential and high current-high

potential. Low current and low potential is ported into the same probe while high current and high potential is ported into another probe as shown in Figure 5.2. Low potential pretends to be ground for the system. Also, applied voltage can be changed with high potential port. The probing is carried out with Cascade M150 Probe Station.

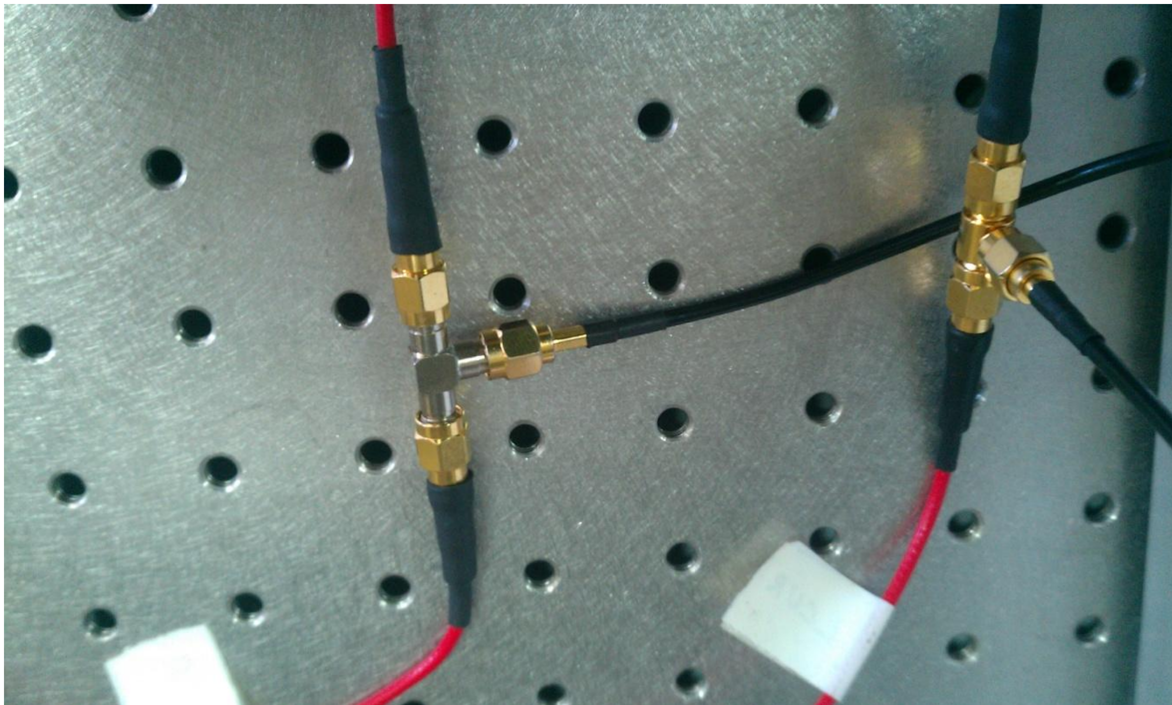

**Figure 5.2**: Low current - low potential and high current - high potential connection. Red cables represent corresponding cables which are connected with black Shape Memory Alloy (SMA) cables via t-connector. By using SMA cables it is aimed to have low noise and low loss.

### 5.1.2. Measurements

All measurements are taken from different devices which are fabricated in the same wafer (see Appendix C). Through Figure 5.3 to Figure 5.5 corresponding results are plotted. Measurements are carried out under same conditions in the same day to conserve

the measurement stability of KEITHLEY 4200. The main concern subjects throughout the measurements are the tendency of capacitance graph, capacitance values and capacitance difference which directly affects force generations in our theoretical calculations.

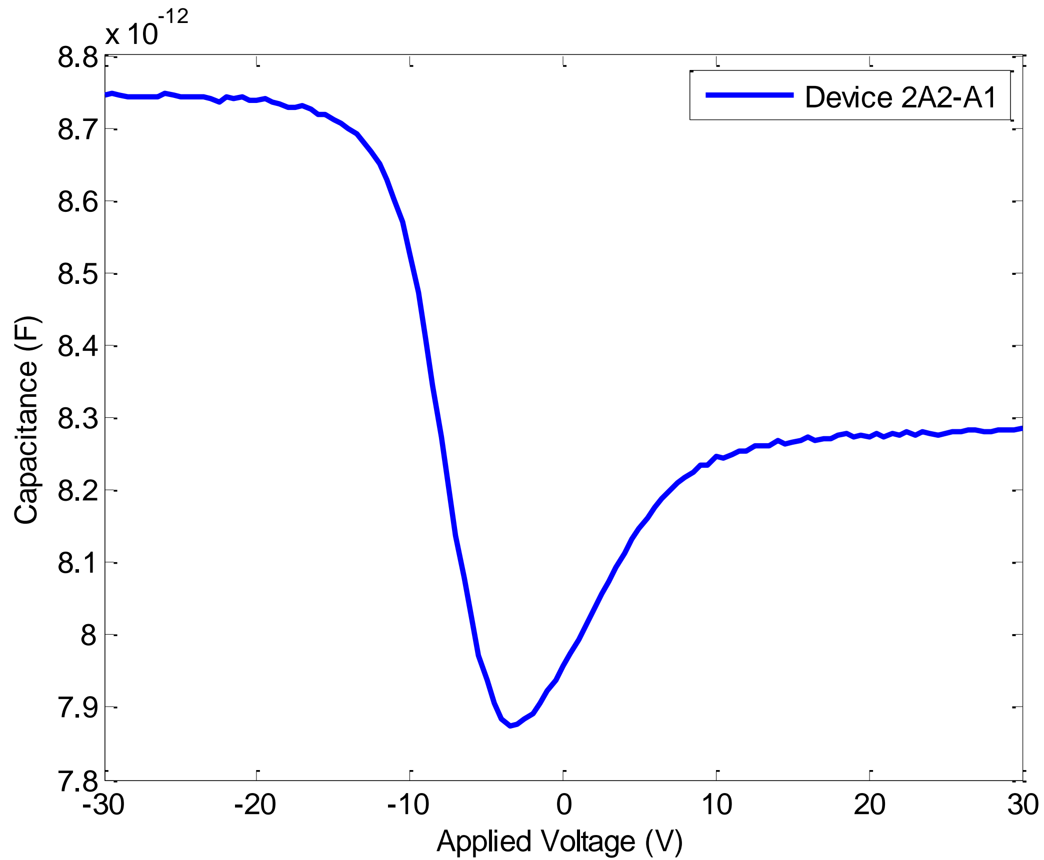


**Figure 5.3**: Capacitance-Voltage measurement of device 2A2-A1 at 1MHz. This device is designed for Si nanowire 2 in Chapter 1.

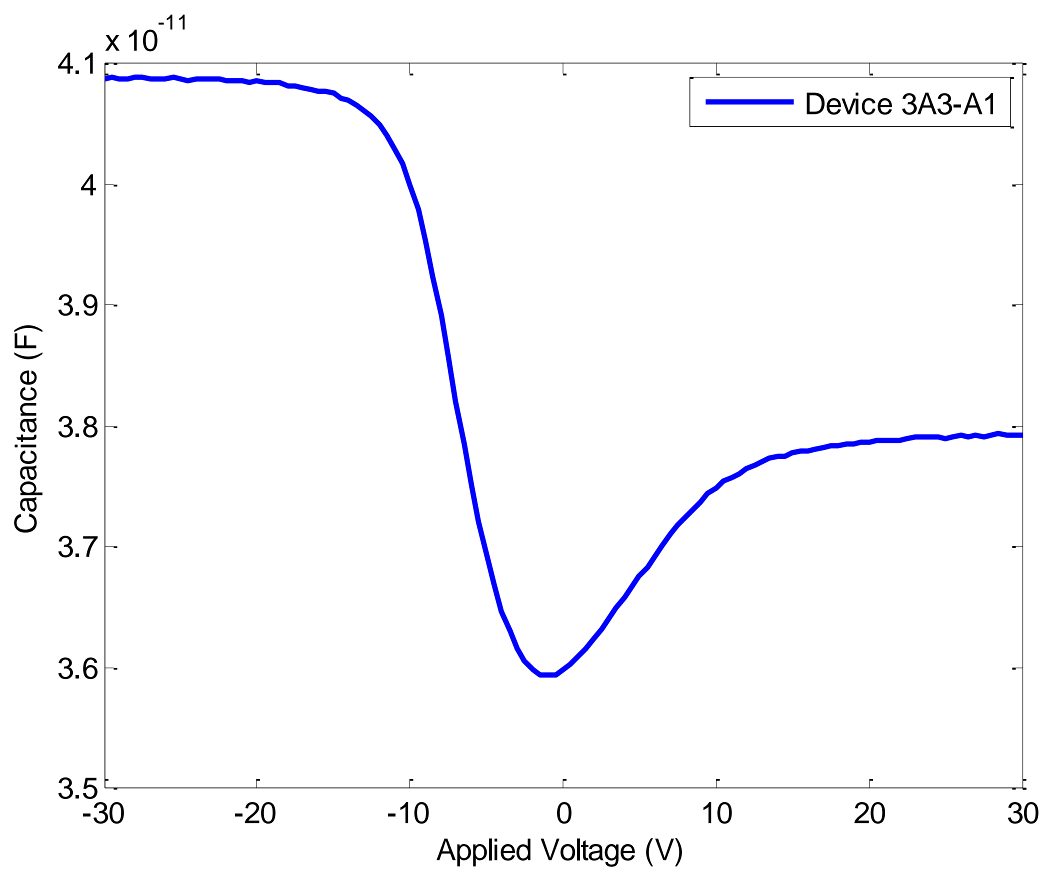


**Figure 5.4**: Voltage-Capacitance measurement of device 3A3-A1 at 1MHz. This device is designed for Si nanowire 3 in Chapter 1.

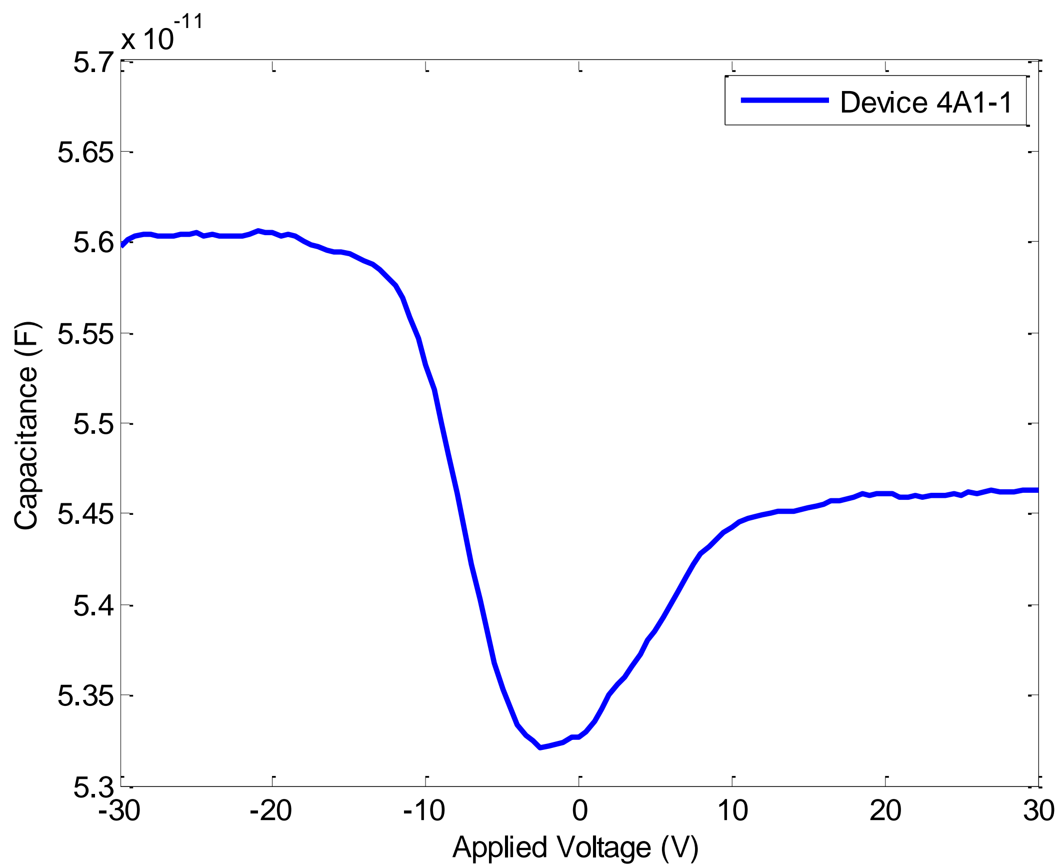


**Figure 5.5**: Voltage-Capacitance measurement of device 4A4-1 at 1MHz. This device is designed for Si nanowire 4 in Chapter 1.

Comparing the results obtained in Figures 5.3, 5.4 and 5.5 with the expected analytical calculations of the corresponding device geometries, we see that the tendency, capacitance values and capacitance difference values are quite different. For a device, while working at negative voltage ranges, graph should give a symmetrical picture with respect to y-axis. This kind of tendency should be the result of electrostatic effect itself. Also we see the minimum capacitance values are at negative voltage. Theoretically, minimum capacitance should be zero voltage if we consider just the device capacitance. Therefore, it demonstrates that there are other effects which deflect our expectations. We think that it might be the result of MOS capacitor which will be discussed in Chapter 6 Parasitic Effects. Next generation devices are designed by including these effects.

### 5.2. Force Sensor Characterization

Force sensor characterization is much more different than actuator. We do not perform a voltage-capacitance analysis but a resonance frequency test and a readout voltage test.

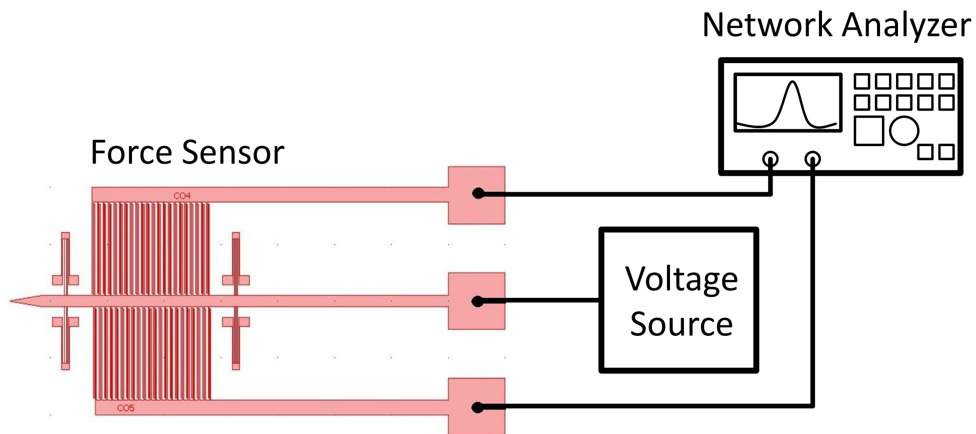


**Figure 5.6:** Resonance frequency measurement setup for force sensor

Figure 5.6 shows the schematic to measure the resonance frequency of the device. Device is connected to a DC voltage source with one port to apply a polarity voltage ($V_p$) and connected to the network analyzer with two ports, one applying an AC voltage and another doing the readout.

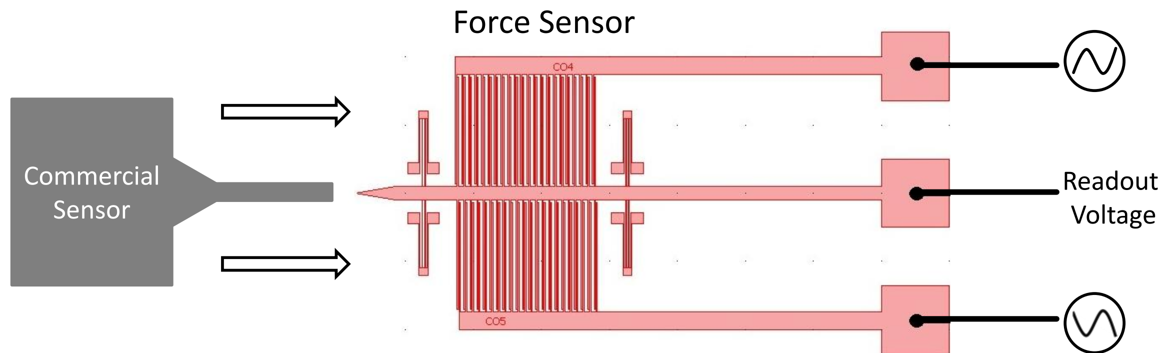


**Figure 5.7:** Schematic for readout voltage measurement for force sensor

Second test for force sensor will be the readout voltage characterization (Figure 5.7). To measure readout voltage, a commercial sensor, whose specifications are known, will be used to push the sensor shuttle. Theoretically, moving shuttle will create a readout voltage due to differential capacitance generation. All touch-pads are designed as RF suitable pads to have lower noise effect on the measurements. GSG touch-pad structure refers to Ground-Signal-Ground. Ground pads serve as shield while "S" port is carrying the signal.

# Chapter 6

# PARASITIC EFFECTS

## 6.1. Introduction

In this chapter, parasitic effects that are encountered during characterization are investigated. Background regarding the problem and method to overcome is discussed and solution for next generation devices is suggested.

## 6.2. Background

The metal oxide semiconductor (MOS) capacitor forms with a metal and a semiconductor material having an insulator layer between them (Figure 6.1). The capacitance of the MOS structure depends on the voltage on the gate. Metallic part is labeled as "gate (G)" while contact to the semiconductor is named as "body (B)". Typically, a voltage is applied to the gate ($V_G$) while the body is grounded.

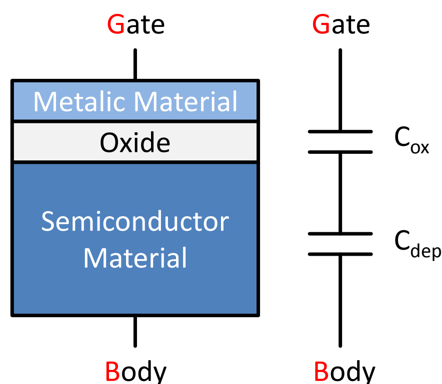


**Figure 6.1:** MOS capacitance representation and lump modeling [24]

The capacitance depends on the voltage that is applied to the gate with respect to the body. Capacitance processing consists of three main regimes separated by two main voltage values. These stages are "Accumulation", "Depletion" and "Inversion" (Figure 6.2). The voltages that bound the regimes are threshold voltage ($V_T$) which separates "Accumulation" and "Depletion", and flatband voltage ($V_{FB}$) which separates "Depletion" and "Inversion".

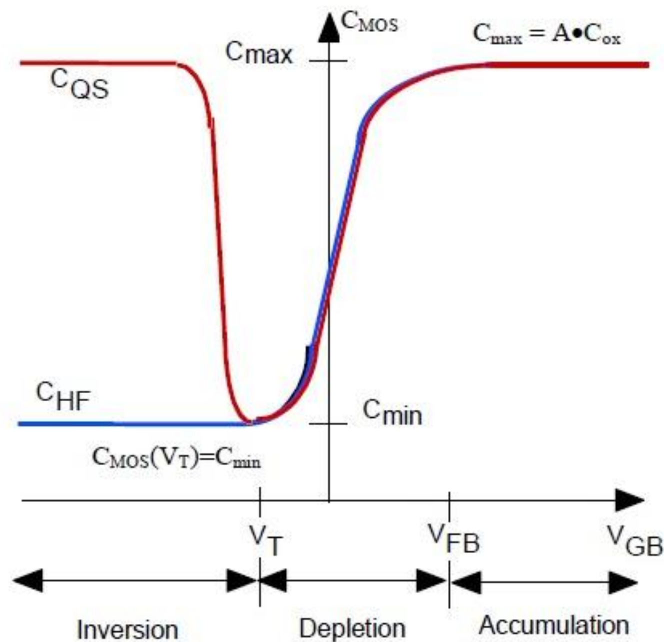


**Figure 6.2:** Gate voltage - capacitance of an n-type MOS capacitor. "A" designates contact area, QS designates quasi-static or low frequency, HF designates high frequency. The unit of the capacitance values in this graph is $F/m^2$. [24]

In Figure 6.2, the flat lined region of the capacitance graph equals to oxide capacitance ($C_{ox}$). The inclined region in "Inversion" regime has both depletion capacitance ($C_{dep}$) and oxide capacitance. Since both capacitances are connected in series in Figure 6.1, the capacitance value in this region is shown in Equation (6.1).

$$C_{MOS} = \frac{C_{ox}C_{dep}}{C_{ox} + C_{dep}} \quad (6.1)$$

If the semiconductor material is n-type meaning that it is doped with phosphor, resulting capacitance will coincide with Figure 6.2. However, changing the doping material type to boron will make the semiconductor p-type. Gate voltage - capacitance graph will become the symmetrical with respect to y-axis when compared to the n-type graph. In Equation (6.2), gate voltage calculation is given in terms of material related properties. $\phi_s$ is surface potential, q is charge, $N_A$ is the substrate doping and $\varepsilon_{si}$ is dielectric constant for Si. In addition, calculating the depletion width with given properties is available in Equation (6.3) and it will lead to find depletion capacitance ($C_{dep}$) in Equation (6.4).

$$V_G = \phi_s + \frac{\sqrt{2qN_A\varepsilon_{si}\phi_s}}{C_{ox}} \quad (6.2)$$

$$w_{dep} = \sqrt{\frac{2\varepsilon_{si}\phi_s}{qN_A}} \quad (6.3)$$

$$C_{dep} = \frac{\varepsilon_{si}A}{w_{dep}} \quad (6.4)$$

### 6.3. Effect in Our Project and Solution

In order to investigate the MOS effect in our devices, a complete lump model of the experiment setup is required. Black-lined capacitance values in Figure 6.3 demonstrate the initial considerations while red-lined capacitances are added after considering MOS effect. Revisiting the Figures 5.3, 5.4 and 5.5 in Chapter 5, the main reason behind the difference between figures and analytical expectation seems to be the oxide and depletion capacitances. Since the depletion capacitance value changes faster than MEMS capacitance, we are not able to detect MEMS capacitance in figures. Figure 6.4 demonstrates the initial and overall lump models designed for our devices.

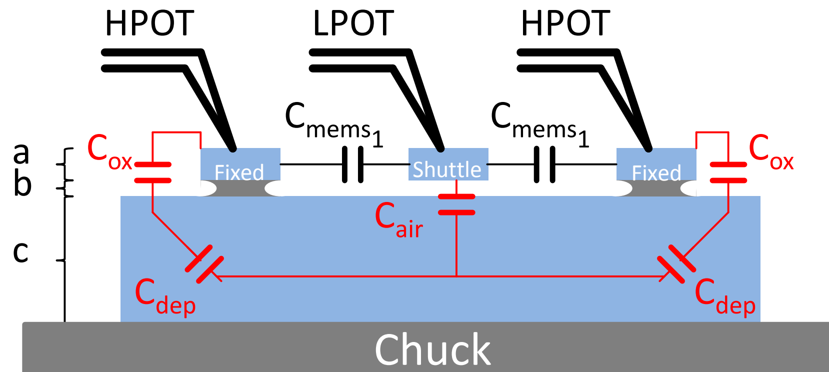


**Figure 6.3:** Actuator CV measurement schematic. a: 10µm Device Layer, b: 1µm BOX Layer, c: 380µm Handle Layer. HPOT: high potential, LPOT: low potential. $C_{mems1}$: MEMS capacitance between one-side wall fingers and shuttle fingers. $C_{air}$: Capacitance between shuttle and handle layer. $C_{ox}$: Oxide capacitance, $C_{dep}$: Depletion capacitance.

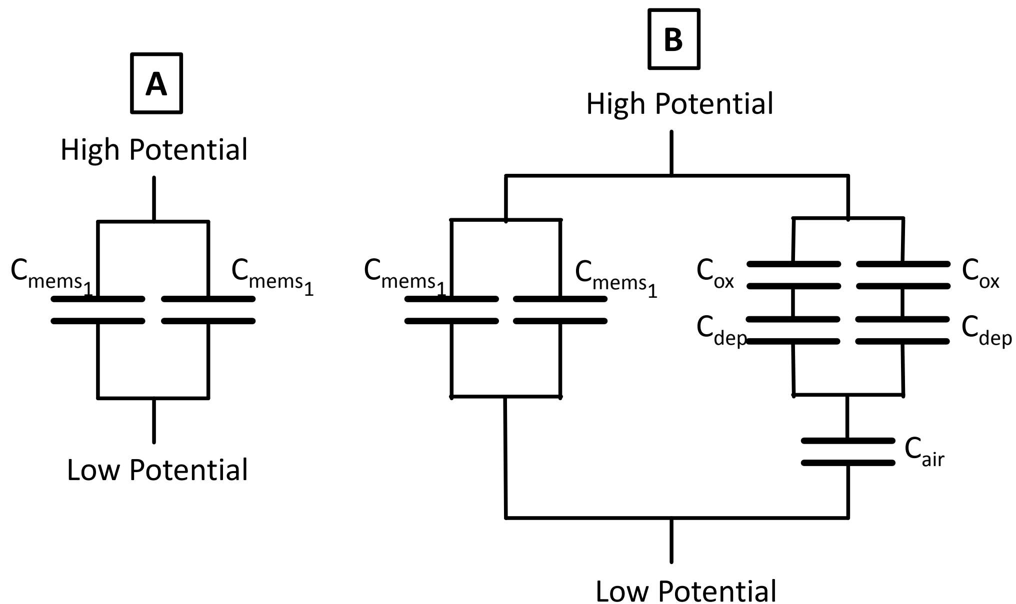


**Figure 6.4:** A: Lump model of first assumption which includes only MEMS capacitance. B: Revised lump model with MOS capacitance effect.

New generation design parameters are found by eventually checking MOS capacitance effect. Our code runs as described in Chapter 2 and 3 until the last point. At the very end of our code (see Appendix A), we add the following steps to take MOS into account. Rather than using directly Equation (6.2), we utilize the solved version of it for $\phi_s$. Placing this value into Equation (6.3) eventuates with depletion width which is needed to calculate depletion capacitance. Finally we find the depletion capacitance with Equation (6.4). To check the stability of device in terms of MOS, overall capacitance ($C_{total}$) in Figure 6.4.B is differentiated in terms of applied voltage (gate voltage - $V_G$). If the relation (6.5) satisfies it is concluded that device overcomes parasitic effect. Also, while finding new device geometries, smaller signal carriage routes are designed to minimize the contact area with the oxide. Decreasing the contact area decreases MOS effect as well.

$$\frac{\partial C_{total}}{\partial V_G} > 0 \tag{6.5}$$

Another way to overcome this effect is playing with the SOI properties. Equations above tell us that there are a few wafer level specifications that are needed. These specifications are substrate doping ($N_A$) and BOX layer thickness. Finding a thicker BOX layer will significantly and directly the oxide capacitance so that equivalent capacitance with depletion capacitance will be more acceptable. $N_A$ is a crucial factor that affects resistivity of the substrate (handle layer). Changing this value also helps to improve the get required design. However, one should do the market availability search for SOI wafers having specific resistivity values. Setting the resistivity value too high or too low might not be reasonable.

One cannot simply dispel the MOS effect completely. What can be done is to reduce its effect with the methods mentioned above or increase the desired output value while still in the design stage. Four our design, we presume the maximum working voltage as 40V so that the resultant capacitance differences is too low to overcome MOS effect.

Reducing the working voltage will definitely help to increase capacitance difference due to the fundamental Equation (2.3) in Chapter 2.

Final step with the MOS is to choose the type of SOI wafer which will be used for fabrication and setting the frequency range. Frequency in this stage is the frequency of the applied voltage to the fixed walls. Figure 6.2 demonstrates the difference between working with a quasi-static voltage signal and a high frequency voltage signal. We prefer to use a p-type SOI wafer and work with quasi-static voltage signal to see the MEMS effect solely, after reaching the threshold voltage. Figure 6.5 indicates the EDS analysis regarding our SOI wafer. P-type SOI wafers should have a significant peak in boron region while having no sign of phosphor. EDS can detect phosphor but simply cannot detect boron completely due being in the limits of the analysis. In the figure, it is seen that there is no phosphor so that wafer is not n-type so that it should be p-type.

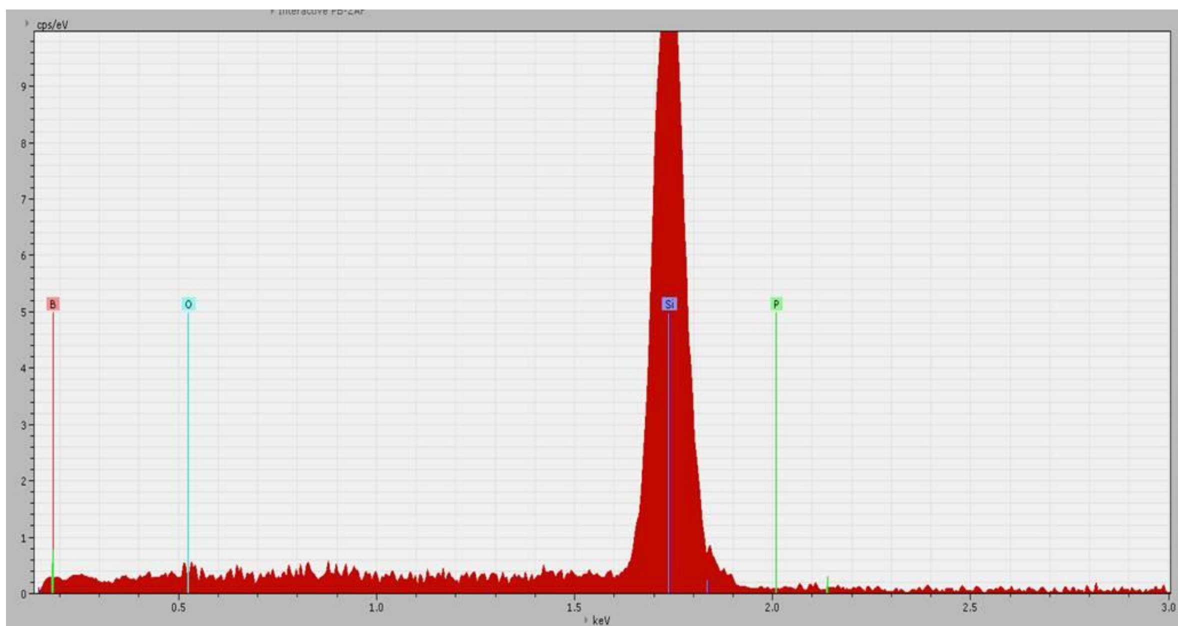


**Figure 6.5:** EDS analysis result of the SOI wafer used for fabrication

# Chapter 7

# CONCLUSION AND FUTURE WORK

This thesis investigates and discusses the needs of a reasonable characterization results for a determined electrostatically actuated MEMS and force sensor, and introduces new geometries and updated fabrication process flow. Applied voltage - capacitance analysis, which is carried out in Boğaziçi University resulted with the dominant effect of MOS capacitance. Hence, geometry parameters for both actuator and force sensor are redesigned. New generation design will have again GSG (Ground - Signal - Ground) - RF touch pads which are 80 μm x 80 μm and have 100 μm center to center distance (suitable for RF probes in Boğaziçi University). RF touch pad provides low noise signal application and more accurate readout.

SOI wafer used during fabrication in this thesis consists of 10 μm device layer, 1 μm BOX layer and 380 μm handle layer. There is no significant elimination but in order to decrease the MOS effect throughout the system, 2 μm BOX will be used and device layer thickness will be kept as the same. Moreover, new SOI wafer will be p-type and more doped which will directly affect the depletion capacitance.

Fabrication steps of both actuator and force sensor will include back side etching. Figure 7.1 demonstrates the proposed fabrication process flow. Succeeding the fabrication and characterization for actuator and force sensor separately is crucial to understand the validity of our estimations and approach. Hence, next step will become monolithic fabrication to overcome interfacial reactions caused by separately connection of sample to

the actuator and sensor. In that stage, Si nanowire fabrication process flow will gain utmost importance to consider a monolithic fabrication.

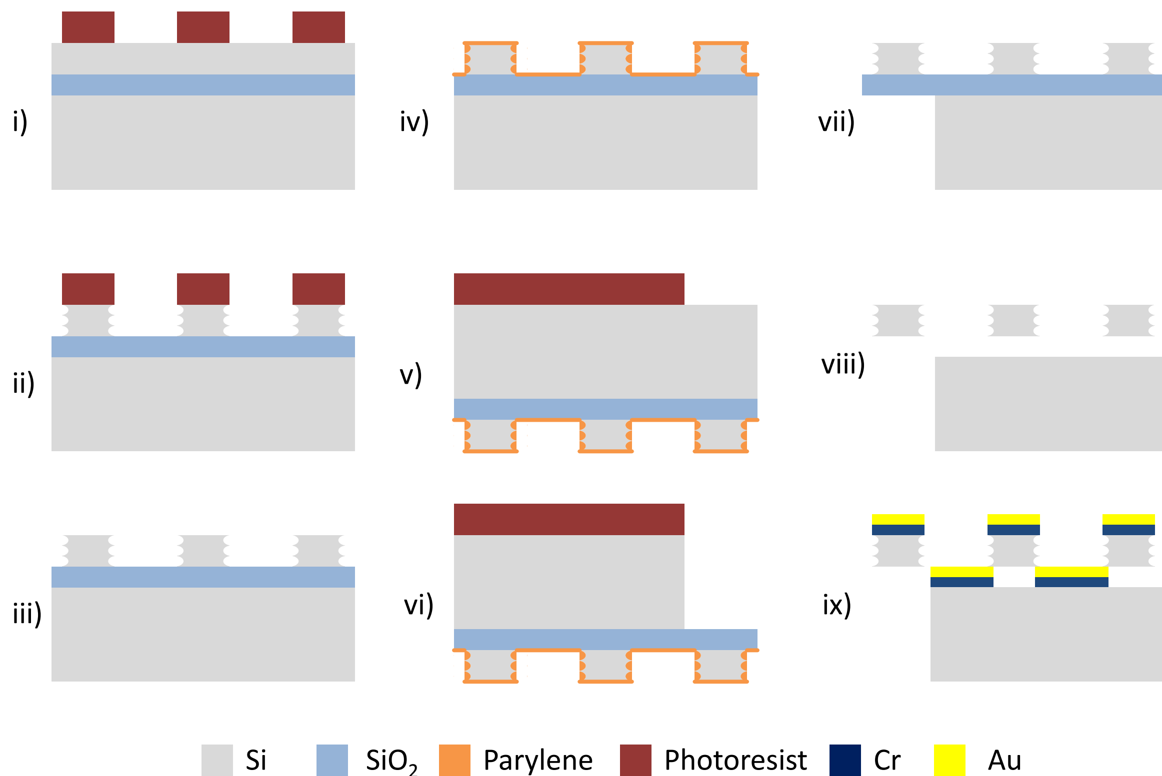


**Figure 7.1:** Revised fabrication process flow for actuator and force sensor. i) Photoresist coating, photolithography and development, ii) BOSCH process, iii) Photoresist strip, iv) Protective layer coating v)Handle layer photoresist coating, photolithography and development, vi) Dry etch, vii) Photoresist strip and scribing, viii) HF vapor release, ix) E-beam evaporation.

# Appendix A

## MATLAB CODE OF THE DESIGN

```
clc
close all
clear all
clc
%% SYSTEM DESIGN FOR MICROTENSILE TESTING OF Si NANOWIRES

%% VARIABLES RELATED TO THE SAMPLE
%% d: NW diameter (m)
%% sigma_f: fracture stress (Pa)
%% asp_rat: aspect ratio
%% A_s: cross-section area of NW (m^2)
%% E: elastic modulus of Si (Pa)
%% K_s: stiffness of the NW (N/m)
%% F_s: force on NW (N)
%% F_smax: max force on NW (N)
%% deltaU_s: elongation of NW (m)
%% epsi_s: strain of NW
%% l_s: initial length of NW (m)

Vol=10^7*1e-27;
d=55*1e-9;
l_s=Vol/(pi*d^2/4);
sigma_f=12*1e9;
A_s=pi*(d^2)/4;
E=170*1e9;
K_s=A_s*E/l_s;
F_smax=sigma_f*A_s;
epsi_s=0.05;
deltaU_s=F_smax/K_s;


% %% VARIABLES RELATED TO THE FORCE SENSOR
% %% epsi_0: permittivity of air
% %% t_fs: thickness of a sensor finger (m)
```

```
% %% w_fs: width of a sensor finger (m)
% %% l_fs: length of a sensor finger (m)
% %% N_data: number of data points
% %% x_fsstep: travel distance of force sensor at one step
(m)
% %% x_fsmax: max travel distance of force sensor (m)
% %% d1: small gap between two fingers (m)
% %% d2: large gap between two fingers (m)
% %% b=d2/d1 ratio
% %% N_fs: number of sensor elements (# of sensor
fingers/3=fix-mov-fix)
% %% deltaC: generated capacitance difference (F)
% %% deltaC_min: minimum capacitance difference (F)
% %% C_total: total capacitance (F)
% %% A_fs: overlapping area of a sensor finger (m^2)
% %% K_fs: stiffness of the force sensor (N/m)
% %% F_fs: force on force sensor (N)
% %% F_fsmax: max force on force sensor (N)
% %% V_fs: voltage applied to force sensor (V)
% %% V_out: voltage read from force sensor (V)
% %% V_outmin: min voltage can be read from analyzer (V)
% %% delta: e.s.force/rest.force ratio (parameter for
stability)
% %% x_fs: travel distance of movable sensor finger (m)
% %% xtilda: x/d1 ratio
% %% xtilda_max: x_fsmax/d1
% %% nl_d: non-linearity due to displacement(deltaC)
(percent)
% %% nl_f: non-linearity due to force(V_fs) (percent)
% %% nl_dmax: max non-lin. due to disp. (percent)
% %% nl_fmax: max non-lin. due to force (percent)
% %% S: sensitivity (V_out/epsi_s)
%
epsi_0=8.854*1e-12;
t_fs=10*1e-6;
w_fs=10*1e-6;
l_fs=780*1e-6;
N_data=2200;
F_fsmax=F_smax;  % Since the force on the NW and the force
sensor is the same.
```

```
d1= 4*1e-6;
b=6;
K_fs=76;
x_fsmax=F_fsmax/K_fs;
S=0;
V_fs=2;  %Voltage applied to the force sensor to read the
differential capacitance.
V_outmin=1*1e-6; % for Agilent 4156A Semiconductor parameter
analyzer
it=1;
N_fs=[0];
A_fs=[0];
nl_dmax=[0];
nl_fmax=[0];

d1val=[0];
d2val=[0];
t_fsval=[0];
w_fsval=[0];
l_fsval=[0];     % In order to take values from the matrices,
'val' operators are written with the parameters.
N_dataval=[0];
K_fsval=[0];
V_fsval=[0];
V_out=[0];
Sval=[0];

% for t_fs=45*1e-6:50*1e-6:145*1e-6
for w_fs=5*1e-6:1e-6:8*1e-6
    for l_fs=100*1e-6:25*1e-6:200*1e-6
        for N_data=1000:100:2000
            for d1=2*1e-6:1*0.25e-6:10*1e-6
                for b=5:0.5:10
                    for K_fs=15:0.5:21
                        for V_fs=2:1:4
                            x_fsmax=F_fsmax/K_fs;
                            d2=b*d1;

                            xtilda_max=x_fsmax/d1;
                            x_fsstep=x_fsmax/N_data;
```

```
                            deltaC_min=1*1e-15; %1fF
                            a=2*epsi_0*(t_fs*l_fs)*x_fsstep;
%to simplify formulas


N_fs(it)=ceil(deltaC_min/(1/(d1^2-x_fsstep^2)-1/(d2^2-
x_fsstep^2))/a);    %ceil operator rounds N_fs to the next
larger integer.

A_fs(it)=N_fs(it)*(d1+d2+2*w_fs)*l_fs;


                            x_fs=0:x_fsstep:x_fsmax;

deltaC=ceil(deltaC_min./(1./(d1.^2-x_fsstep^2)-1./(d2.^2-
x_fsstep^2))/a)*2*epsi_0*(t_fs*l_fs)*x_fs.*(1./(d1.^2-
x_fs.^2)-1./(d2.^2-x_fs.^2));

                            %% Force sensor ARDE analysis

                            asp_rat_fs=45;
                            if t_fs/d1>asp_rat_fs
                                continue
                            end
                            %% Force sensor fringing field
analysis

                            if xtilda_max>0.5
                                continue
                            end

                            %% Force sensor simplicity
analysis

                            if N_fs(it)>2000
                                continue
                            end

                            %% Force sensor stability
analysis
```

```
delta=2*N_fs(it)*epsi_0*(t_fs*l_fs)*V_fs^2/(K_fs*d1^3);

                            xtilda=0:1e-2:1;
                            ind=length(xtilda);
                            f=xtilda.*(1-delta*(1./(b^3*(1-
xtilda.^2/b^2).^2)+(1./(1-xtilda.^2).^2)));

                            peak=max(f);
                            for i=1:ind
                                if f(i)==peak
                                    peakx=i;
                                end
                            end

                            if peakx/100<xtilda_max
                                continue
                            end

                            %% Force sensor linearity
analysis

                            %

xtilda=linspace(0,xtilda_max,100);


nl_d=(xtilda/xtilda_max).*((1./(1-xtilda.^2)-1./(b^2-
xtilda.^2))/(1/(1-xtilda_max^2)-1/(b^2-xtilda_max^2))-1);

nl_f=(xtilda/xtilda_max).*((1./(1-xtilda.^2)-1./(b^2-
xtilda.^2))/(1/(1-xtilda_max^2)-1/(b^2-xtilda_max^2))-(1-
delta*(b./(b^2-xtilda.^2).^2+1./(1^2-xtilda.^2).^2))*1./(1-
delta*(b./(b^2-xtilda_max.^2).^2+1./(1^2-xtilda_max.^2)^2)));

                            nl_dmax(it)=max(abs(nl_d));
                            nl_fmax(it)=max(abs(nl_f));

                            if nl_fmax(it)>0.05
```

```
                                    continue
                                end

                                %% Force sensor finger stability
analysis

                                safety=3;

fingerdisp=safety*3*l_fs^5*epsi_0*V_fs^2*(d2/(d2^2-
x_fsmax^2)^2+d1/(d1^2-x_fsmax^2)^2)*x_fsmax/(E*w_fs^3);

                                if fingerdisp>(d1-x_fsmax)
                                    continue
                                end

                                %% Output voltage(V_out) analysis


C_total(it)=ceil(deltaC_min./(1./(d1.^2-x_fsstep^2)-
1./(d2.^2-x_fsstep^2))/a)*epsi_0*l_fs*t_fs*(1/d1+1/d2)*2;


V_out(it)=max(deltaC)/C_total(it)*V_fs;

                                if V_out(it)<V_outmin*N_data
                                    continue
                                end
                                %% Microtensile tester
sensitivity analysis


S=V_out(it)./((x_fsmax*K_fs/K_s)/l_s);


                                %fprintf(fid, '%6.2e %6.2e %6.2e
%6.2e %6.2e %6.2e %6.2e %6.2e %6.2e %6.2e
%6.2e\n',t_fs,w_fs,l_fs,N_data,d1,d2,K_fs,V_out(it),N_fs(it),
A_fs(it)*1e6,nl_fmax(it)*100);

                                d1val(it)=d1;
```

```
                            d2val(it)=d2;
                            t_fsval(it)=t_fs;
                            w_fsval(it)=w_fs;
                            l_fsval(it)=l_fs;
                            N_dataval(it)=N_data;
                            K_fsval(it)=K_fs;
                            V_fsval(it)=V_fs;
                            Sval(it)=S;

                            it=it+1;
                            %
ForceSensorTable(d,t_fsval,w_fsval,l_fsval,N_dataval,d1val,d2
val,K_fsval,V_fsval,N_fs,A_fs,nl_fmax,Sval);

                        end
                    end
                end
            end
        end
    end
end
% end

FST(d,t_fsval,w_fsval,l_fsval,N_dataval,d1val,d2val,K_fsval,V
_fsval,N_fs,A_fs,nl_fmax,Sval);

%% VARIABLES RELATED TO THE FORCE SENSOR SPRINGS
%% K_fs: force sensor stiffness (N/m)
%% t_kfs: thickness of sensor spring finger (m)
%% w_kfs: width of sensor spring finger (m)
%% l_kfs: length of sensor finger (m)
%% N_kfs: number of sensor springs
%% K_kfs: sensor spring stiffness (N/m)
%% K_kfsy: sensor spring stiffness along y-direction (N/m)
%% K_kfsz: sensor spring stiffness along z-direction (N/m)

K_fs=9.5;
% K_kfsval=[0];
% K_kfs=K_fs;
% t_kfs=10*1e-6;
```

```
% w_kfsval=[0];
% l_kfs1val=[0];
% l_kfs2val=[0];
% asprat1fsval=[0];
% asprat2fsval=[0];
% i=1;

% for w_kfs=5*1e-6:1e-6:15*1e-6
%     for l_kfs1=10*1e-6:5*1e-6:500*1e-6
%         for l_kfs2=20*1e-6:5*1e-6:500*1e-6
%             K_kfs=8*E*t_kfs*w_kfs^3/(l_kfs1^3+l_kfs2^3);
%
%             if l_kfs1-l_kfs2<100*1e-6
%                 continue
%             end
%
%             if l_kfs1/w_kfs>100 || l_kfs2/w_kfs>100
%                 continue
%             end
%
%             if K_kfs>100 || K_kfs<50
%                 continue
%             end
%             l_kfs1val(i)=l_kfs1;
%             l_kfs2val(i)=l_kfs2;
%             w_kfsval(i)=w_kfs;
%             K_kfsval(i)=K_kfs;
%             asprat1fsval(i)=l_kfs1val(i)/w_kfsval(i);
%             asprat2fsval(i)=l_kfs2val(i)/w_kfsval(i);
%             i=i+1;
%         end
%     end
% end
%
%
FSKT(t_kfs,w_kfsval,l_kfs1val,l_kfs2val,K_kfsval,asprat1fsval
,asprat2fsval);

%
%
```

```
% VARIABLES RELATED TO THE ACTUATOR SPRINGS
% K_a: actuator stiffness (N/m)
% t_ka: thickness of actuator spring finger (m)
% w_ka: width of actuator spring finger (m)
% l_ka: length of actuator spring finger (m)
% N_ka: number of actuator springs
% K_ka: actuator spring stiffness (N/m)
% K_kay: actuator spring stiffness along y-direction (N/m)
% K_kaz: actuator spring stiffness along z-direction (N/m)
%
t_ka=10*1e-6;
w_ka=5*1e-6;
l_ka1=500*1e-6;
l_ka2=400*1e-6;

% w_kaval=[0];
% l_ka1val=[0];
% l_ka2val=[0];
% K_kaval=[0];
% asprat1val=[0];
% asprat2val=[0];
% i=1;
% z=1;
% for w_ka=5e-6:1e-6:10e-6
%     for l_ka1=200e-6:1e-6:700e-6
%         for l_ka2=200e-6:1e-6:700e-6
%
%             K_ka=4*E*t_ka*w_ka^3/(l_ka1^3+l_ka2^3);
%             z=z+1
%             if l_ka1-l_ka2<30*1e-6
%                 continue
%             end
%
%             if l_ka1/w_ka>100 || l_ka2/w_ka>100
%                 continue
%             end
%
%             if K_ka>10.5 || K_ka<9.6
%                 continue
%             end
```

```
%               l_ka1val(i)=l_ka1;
%               l_ka2val(i)=l_ka2;
%
%               w_kaval(i)=w_ka;
%               K_kaval(i)=K_ka;
%               asprat1val(i)=l_ka1val(i)/w_kaval(i);
%               asprat2val(i)=l_ka2val(i)/w_kaval(i);
%
%               i=i+1;
%
%           end
%       end
% end


K_kaz=4*E*w_ka*t_ka^3/(l_ka1^3+l_ka2^3);
K_ay=4*E*w_ka*t_ka/(l_ka1+l_ka2);
K_a=4*E*t_ka*w_ka^3/(l_ka1^3+l_ka2^3);
K_fs=76;
% AST(t_ka,w_kaval,l_ka1val,l_ka2val,K_kaval);
% % K_a=6.27;
%
% VARIABLES RELATED TO THE ACTUATOR
% epsi_0: air permittivity
% t_a: thickness of actuator finger (m)
% w_a: width of actuator finger (m)
% h: zero voltage overlap of actuator finger (m)
% gx: gap between actuator fingers in x-direction (tip of
finger) (m)
% gy: gap between actuator fingers in y-direction (actuation
gap) (m)
% gz: gap between testing device and handle layer (m)
% V_a: applied voltage (V)
% V_amax: max applied voltage (V)
% x_a: displacement of actuator finger (m)
% x_amax: max displacement of actuator finger (m)
% F_e: generated electrostatic force (N)
% F_emax: max generated electrostatic force (N)
% F_a: force at the tip of the actuator (transferred to
actuator springs) (N)
```

```
% N_a: number of actuator fingers
% A_a: area of the actuator
% K_a: actuator stiffness (N/m)
% V_pix: pull-in voltage for front pull-in (V)
% V_piy: pull-in voltage for side pull-in (V)
% V_piz: levitation pull-in voltage (V)
% K_eq: equivalent stiffness of whole system (N/m)
% x_pi: pull-in distance (m)

K_a=4;
t_a=10*1e-6;
w_a=5*1e-6;
h=6*1e-6;
gx=96*1e-6;
gy=4*1e-6;
gz=2*1e-6;
V_amax=20;
N_a=[0];
A_a=[0];
A_a2=[0];
fin_sol=[0];
ir=1;
t_aval=[0];
w_aval=[0];
gxval=[0];
gyval=[0];
hval=[0];
V_pix=[0];
Vmax=[0];
ratio=[0];
Cap_arr=[0];
Cap_dif=[0];
Cox=[0];
fark=0;

for t_a=45*1e-6:50*1e-6:145*1e-6
for V_amax=[10 15 14 13 12 20]
difference=1;
for V_amax=[25]
for w_a=5*1e-6:1e-6:8*1e-6
```

```
    for gx=5*1e-6:5*1e-6:100*1e-6
        for gy=1.5*1e-6:0.5*1e-6:3*1e-6
            for h=6*1e-6:2e-6:100*1e-6

                x_amax=deltaU_s+x_fsmax;

                if h+x_amax>gx
                    continue
                end

                while gx<x_amax
                    gx=gx+1e-6;
                end

                K_eq=(K_fs*K_s+K_a*K_s+K_a*K_fs)/(K_fs+K_s);

                F_emax=F_smax/((K_s*K_fs)/(K_s+K_fs))*K_eq;
                N_a(ir)=ceil(F_emax/(epsi_0*t_a*(w_a/(gx-
x_amax)^2+1/gy)*V_amax^2));
                A_a(ir)=(2*gx+h)*2*(gy+w_a)*N_a(ir);


                Actuator ARDE analysis

                asp_rat_a=45;

                if asp_rat_a<t_a/gy
                    continue
                end

                Actuator simplicity analysis

                if N_a(ir)>2000
                    continue
                end

                Actuator stability analysis----Front pull-in

                x_pi1=gx + ((3*gx^3)/2 - (gx*(3*gx^2 +
3*gy*w_a))/2 + (((3*gx^3)/2 - (gx*(3*gx^2 + 3*gy*w_a))/2 +
```

```
(gx*gy*w_a)/2)^2 + gy^3*w_a^3)^(1/2) + (gx*gy*w_a)/2)^(1/3) -
(gy*w_a)/((3*gx^3)/2 - (gx*(3*gx^2 + 3*gy*w_a))/2 +
(((3*gx^3)/2 - (gx*(3*gx^2 + 3*gy*w_a))/2 + (gx*gy*w_a)/2)^2
+ gy^3*w_a^3)^(1/2) + (gx*gy*w_a)/2)^(1/3);
                x_pi2=gx + (3^(1/2)*(((3*gx^3)/2 -
(gx*(3*gx^2 + 3*gy*w_a))/2 + (((3*gx^3)/2 - (gx*(3*gx^2 +
3*gy*w_a))/2 + (gx*gy*w_a)/2)^2 + gy^3*w_a^3)^(1/2) +
(gx*gy*w_a)/2)^(1/3) + (gy*w_a)/((3*gx^3)/2 - (gx*(3*gx^2 +
3*gy*w_a))/2 + (((3*gx^3)/2 - (gx*(3*gx^2 + 3*gy*w_a))/2 +
(gx*gy*w_a)/2)^2 + gy^3*w_a^3)^(1/2) +
(gx*gy*w_a)/2)^(1/3))*i)/2 - ((3*gx^3)/2 - (gx*(3*gx^2 +
3*gy*w_a))/2 + (((3*gx^3)/2 - (gx*(3*gx^2 + 3*gy*w_a))/2 +
(gx*gy*w_a)/2)^2 + gy^3*w_a^3)^(1/2) + (gx*gy*w_a)/2)^(1/3)/2
+ (gy*w_a)/(2*((3*gx^3)/2 - (gx*(3*gx^2 + 3*gy*w_a))/2 +
(((3*gx^3)/2 - (gx*(3*gx^2 + 3*gy*w_a))/2 + (gx*gy*w_a)/2)^2
+ gy^3*w_a^3)^(1/2) + (gx*gy*w_a)/2)^(1/3));
                x_pi3=gx - (3^(1/2)*(((3*gx^3)/2 -
(gx*(3*gx^2 + 3*gy*w_a))/2 + (((3*gx^3)/2 - (gx*(3*gx^2 +
3*gy*w_a))/2 + (gx*gy*w_a)/2)^2 + gy^3*w_a^3)^(1/2) +
(gx*gy*w_a)/2)^(1/3) + (gy*w_a)/((3*gx^3)/2 - (gx*(3*gx^2 +
3*gy*w_a))/2 + (((3*gx^3)/2 - (gx*(3*gx^2 + 3*gy*w_a))/2 +
(gx*gy*w_a)/2)^2 + gy^3*w_a^3)^(1/2) +
(gx*gy*w_a)/2)^(1/3))*i)/2 - ((3*gx^3)/2 - (gx*(3*gx^2 +
3*gy*w_a))/2 + (((3*gx^3)/2 - (gx*(3*gx^2 + 3*gy*w_a))/2 +
(gx*gy*w_a)/2)^2 + gy^3*w_a^3)^(1/2) + (gx*gy*w_a)/2)^(1/3)/2
+ (gy*w_a)/(2*((3*gx^3)/2 - (gx*(3*gx^2 + 3*gy*w_a))/2 +
(((3*gx^3)/2 - (gx*(3*gx^2 + 3*gy*w_a))/2 + (gx*gy*w_a)/2)^2
+ gy^3*w_a^3)^(1/2) + (gx*gy*w_a)/2)^(1/3));

                Soln=[x_pi1,x_pi2,x_pi3];

                for index=1:length(Soln)
                    if imag(Soln(index))~=0
                        Soln(index)=-1;
                    end
                end


                Soln=sort(Soln);
```

```
                if min(Soln)>=0
                    fin_sol(ir)=min(Soln);
                end

                if min(Soln)<0
                    for index2=1:(length(Soln)-1)
                        if Soln(index2)<=0  &&
Soln(index2+1)>0
                            fin_sol(ir)=Soln(index2+1);
                        end
                    end
                end

                if x_amax>fin_sol(ir)
                    frontpullin=fin_sol(ir);
                    continue
                end


V_pix(ir)=(fin_sol(ir)*K_eq/(epsi_0*t_a*(w_a/(gx-
fin_sol(ir))^2+1/gy)*N_a(ir))).^0.5;

                if V_pix(ir)-V_amax<1
                    continue
                end


                Actuator stability analysis----Side pull-in

                safety=4;

V_piy=safety*(K_ay*gy^3/(2*N_a(ir)*epsi_0*t_ka*(x_amax+h)))^.
5;

                if V_amax>V_piy
                    sidepullin=V_piy;
                    continue
                end
```

```
                Actuator linearity analysis

                if (h+x_amax)/gy*(gx-x_amax)/w_a<40
                    continue
                end

                Actuator levitation (out-of-plane motion)
analysis

                A_a2(ir)=2*(gx+h)*(w_a)*N_a(ir);

V_piz=sqrt(8*K_kaz*gz^3/(27*epsi_0*A_a2(ir)/2));   %Can be
written on the table.


                Capacitance vs Voltage

                   t=t_a;
                   w=w_a;
                   k=K_a;
                   V=V_amax;
                   N=N_a(ir);
                   eps=epsi_0;

            %% Un-comment this part for only 0-V_amax Volts
% % Capacitance vs Applied Voltage Calculation and Graph.
Enter variables. Run by only selecting
% % this part (Press F9 after selection !)

                 t=t_a;
                 w=w_a;
                 gx=gx;
                 gy=gy;
                 h=h;
                 k=K_a;
                 Volt=V_amax;
                 N=N_a;
                 eps=epsi_0;

                 for iter=1:Volt+1
```

```
                    V=iter-1;
                    A=(2*(gx*gy*k-eps*N*t*V^2)^3-
27*eps*gy^3*k^2*N*t*V^2*w+3*sqrt(3)*sqrt(eps*gy^3*k^2*N*t*V^2
*w*(4*(-
gx*gy*k+eps*N*t*V^2)^3+27*eps*gy^3*k^2*N*t*V^2*w)))^(1/3);
                    r=1/(6*gy*k)*(4*gx*gy*k+2*eps*N*t*V^2-
(2*2^(1/3)*(gx*gy*k-eps*N*t*V^2)^2)/(A)-2^(2/3)*A);
                    root(iter)=real(r);
                end

                Cap=2*N*eps*t*(w./(gx-
root)+(h+root)/gy)*1e15;

%                 figure(1)
%
subplot(3,1,1),plot(0:1:V_amax,root,'linewidth',3),xlabel('Vo
ltage Applied (V)'),ylabel('Displacement (m)'),title('Voltage
applied to the Actuator - Displacement of Actuator')
%
subplot(3,1,2),plot(0:1:V_amax,Cap,'linewidth',3),xlabel('Vol
tage Applied (V)'),ylabel('Capacitance (C)'),title('Voltage
applied to the Actuator - Capacitance of Actuator')
%                 subplot(3,1,3),plot(0:1:V_amax,Cap-
Cap(1),'linewidth',3),xlabel('Voltage Applied
(V)'),ylabel('Capacitance (C)'),title('Voltage applied to the
Actuator - Capacitance Difference of Actuator')


                  A=(2*(gx*gy*k-eps*N*t*V^2)^3-
27*eps*gy^3*k^2*N*t*V^2*w+3*sqrt(3)*sqrt(eps*gy^3*k^2*N*t*V^2
*w*(4*(-
gx*gy*k+eps*N*t*V^2)^3+27*eps*gy^3*k^2*N*t*V^2*w)))^(1/3);
                  r=1/(6*gy*k)*(4*gx*gy*k+2*eps*N*t*V^2-
(2*2^(1/3)*(gx*gy*k-eps*N*t*V^2)^2)/(A)-2^(2/3)*A);
                  root=real(r);

                  Cap=2*N*eps*t*(w/(gx-
root)+(h+root)/gy)*1e15;
                  Cap_0=2*N*eps*t*(w/gx+h/gy)*1e15;
                  Cap_arr(ir)=Cap;
```

```
                    Cap_0_arr(ir)=Cap_0;
                    Cap_dif(ir)=Cap_arr(ir)-Cap_0_arr(ir);

                    area=2*2*(gy+w)*N*30e-6;
                    epsilon_r=3.9;
                    gap=2e-6;
                    C_ox=epsilon_r*epsi_0*area/gap;
                    area_air=N*w_a*(gx+h)*2;
                    Cair=epsi_0*area_air/gap;

                    Cox(ir)=C_ox;
                    ratio(ir)=C_ox/Cap;
                    Vmax(ir)=V_amax;

                    %% parasitic cap vs mems cap difference
control
                    x=2e-6;
                    e_si=11.68;
                    e_sio2=3.9;
                    e_0=8.854e-12;
                    q=1.6e-19;
                    NA=10e16*1e6;

                    t=t_a;
                    w=w_a;
                    k=K_a;
                    eps=epsi_0;

                    Vmax(ir)=V_amax;
                    pullx=fin_sol(ir);

                    V_arr=linspace(0.1,V_amax,40);
                    for iter=1:1:length(V_arr)

                        V=V_arr(iter);


r=(1/(6*gy*k))*(4*gx*gy*k+2*eps*N*t*V^2-(2*2^(1/3)*(gx*gy*k-
eps*N*t*V^2)^2)/(2*(gx*gy*k-eps*N*t*V^2)^3-
27*eps*gy^3*k^2*N*t*V^2*w+3*sqrt(3)*sqrt(eps*gy^3*k^2*N*t*V^2
```

```
*w*(4*(-
gx*gy*k+eps*N*t*V^2)^3+27*eps*gy^3*k^2*N*t*V^2*w)))^(1/3)-
2^(2/3)*(2*(gx*gy*k-eps*N*t*V^2)^3-
27*eps*gy^3*k^2*N*t*V^2*w+3*sqrt(3)*sqrt(eps*gy^3*k^2*N*t*V^2
*w*(4*(-
gx*gy*k+eps*N*t*V^2)^3+27*eps*gy^3*k^2*N*t*V^2*w)))^(1/3));
                       root(iter)=real(r);

                       if root(iter)>=pullx
                           Vmax(ir)=V_arr(iter-1);
                           break;
                       end

                       mems_cap(iter)=2*N*eps*t*(w/(gx-
root(iter))+(h+root(iter))/gy);
                       mems_cap(iter)=2*N*eps*t*(w/(gx-
root(iter))+(h+root(iter))/gy);

                       B2(iter) = (V*e_0*e_sio2^2 -
x*(NA*e_si*q*(2*V*e_0*e_sio2^2 + NA*e_si*q*x^2))^(1/2) +
NA*e_si*q*x^2)/(e_0*e_sio2^2);

w2(iter)=sqrt(2*e_si*e_0*B2(iter)/(q*NA));
                       C_dep(iter)=e_si*e_0*area/w2(iter);

C_para(iter)=C_ox*C_dep(iter)/(C_ox+C_dep(iter));

Ctot(iter)=mems_cap(iter)+C_dep(iter)*C_ox*Cair/(C_ox*C_dep(i
ter)+Cair*C_dep(iter)+C_ox*Cair);

                   end

                   for ind=1:iter-1-1

                       Cdif(ind)=Ctot(ind+1)-Ctot(ind);
                       ind;
                       if Cdif(ind)<-1e-15
                           difference=0;
                           asdsada=0;
```

```
                                break;
                            end
                        end
                        if difference==0
                            continue;
                        end

                        fark=fark+1

                        ratio(ir)=[0];
                        Cap_arr(ir)=[0];
                        Cap_dif=[0];
                        Cox(ir)=C_ox;


                        gxval(ir)=gx;
                        gyval(ir)=gy;
                        hval(ir)=h;
                        w_aval(ir)=w_a;
                        t_aval(ir)=t_a;
                        Cap_dif(ir)=0;
                        ir=ir+1;
                        length(N_a);
                end
            end
        end
    end
end
end

ActuatorTable(d,t_aval,w_aval,hval,gxval,gyval,K_a,V_amax,N_a
,A_a);


ACT(d,t_aval,w_aval,hval,gxval,gyval,K_a,Vmax,N_a,A_a,Cap_arr
,Cox,ratio,Cap_dif);
```

# Appendix B

## SEM IMAGES OF FABRICATED ACTUATORS AND TEST WAFER CHARACTERIZATION

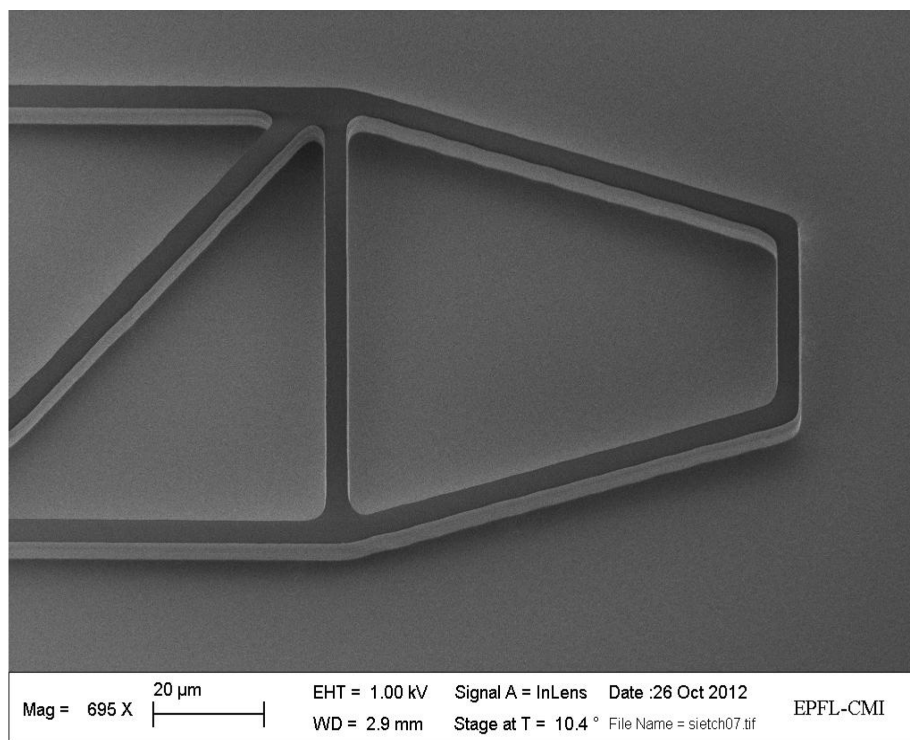


**Figure B.1:** Actuator tip

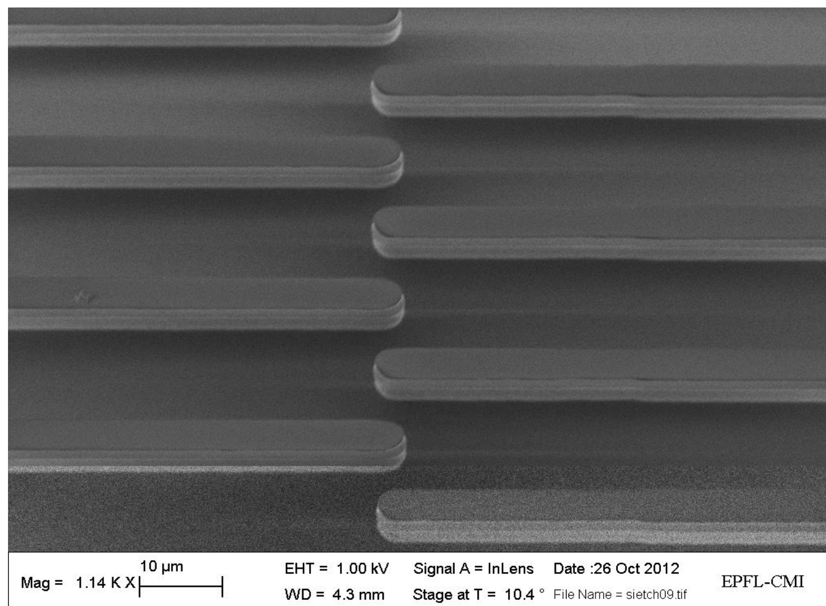


**Figure B.2:** Actuator fingers

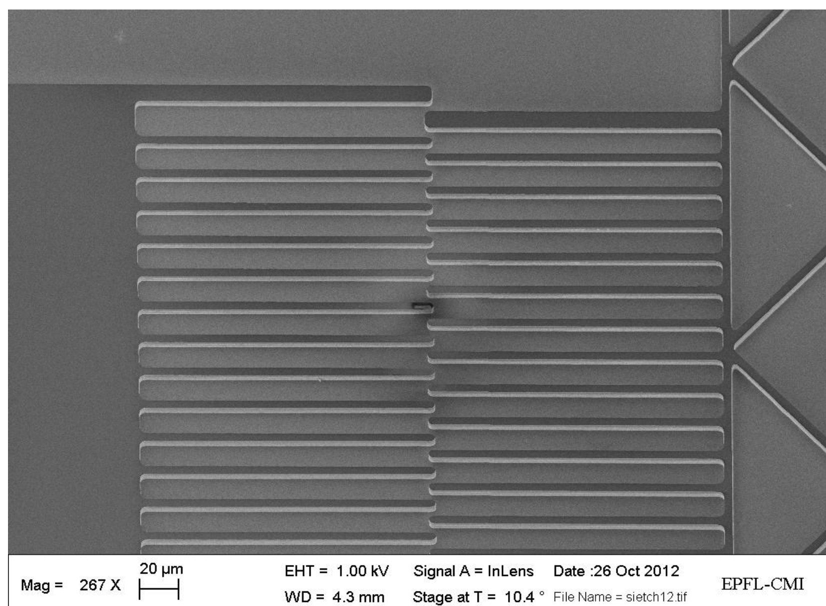


**Figure B.3:** Actuator fingers

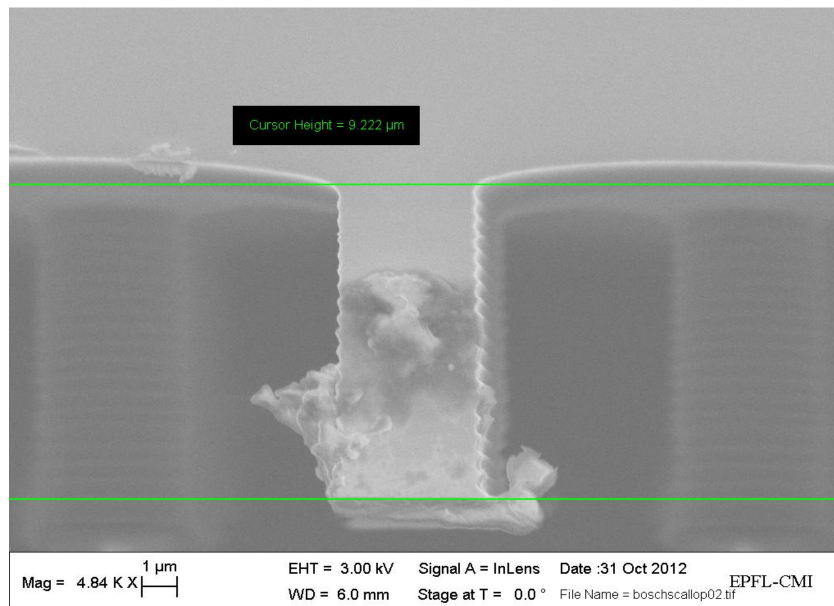


**Figure B.4:** Actuator finger cross-sectional view, Si test wafer

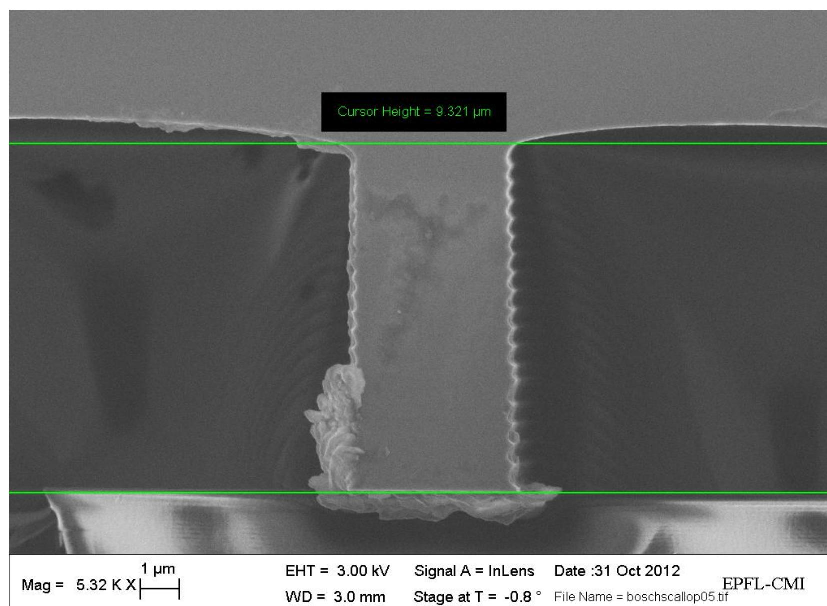


**Figure B.5:** Actuator finger cross-sectional view, Si test wafer

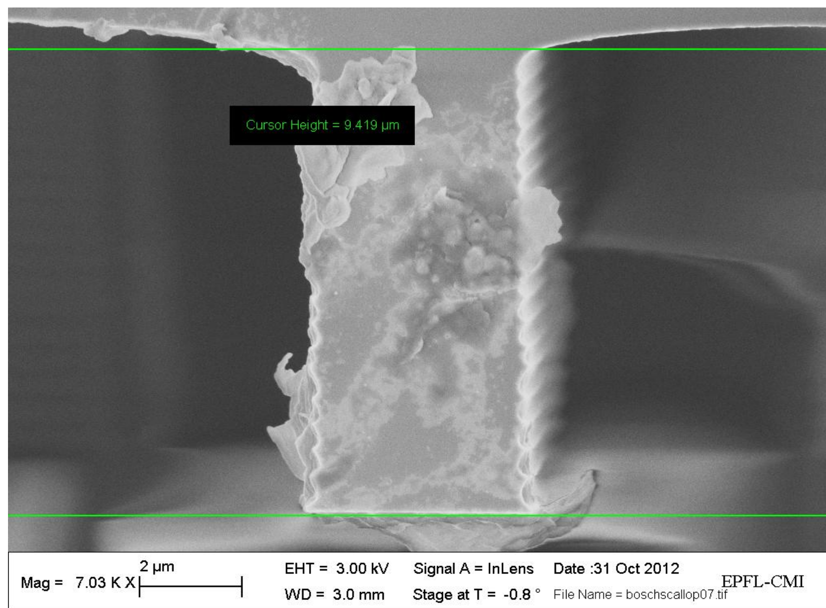


**Figure B.6:** Actuator finger cross-sectional view, Si test wafer

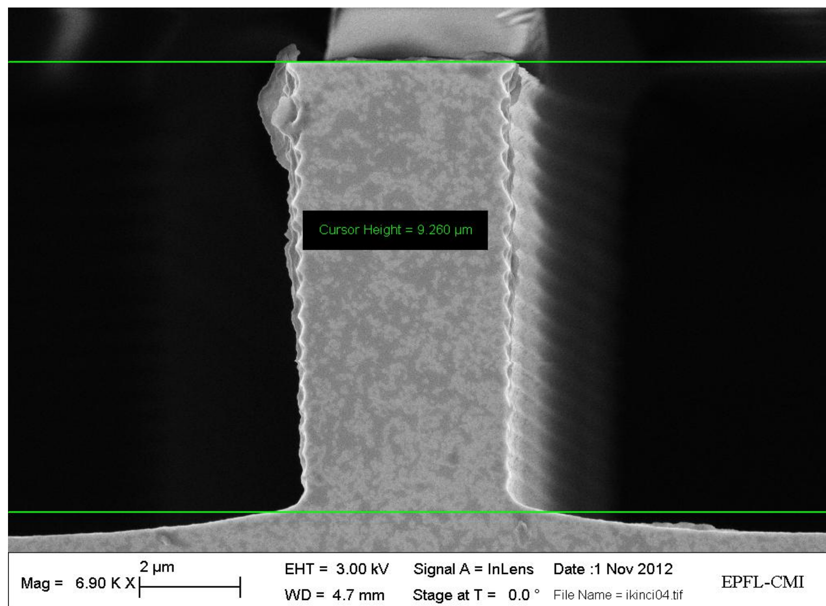


**Figure B.7:** Actuator finger cross-sectional view, Si test wafer

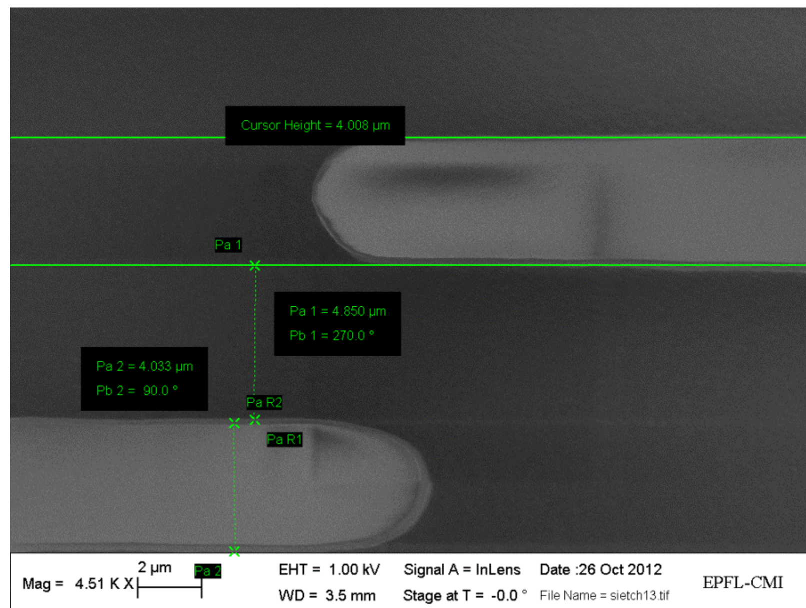


**Figure B.8:** Actuator finger top view, Si test wafer

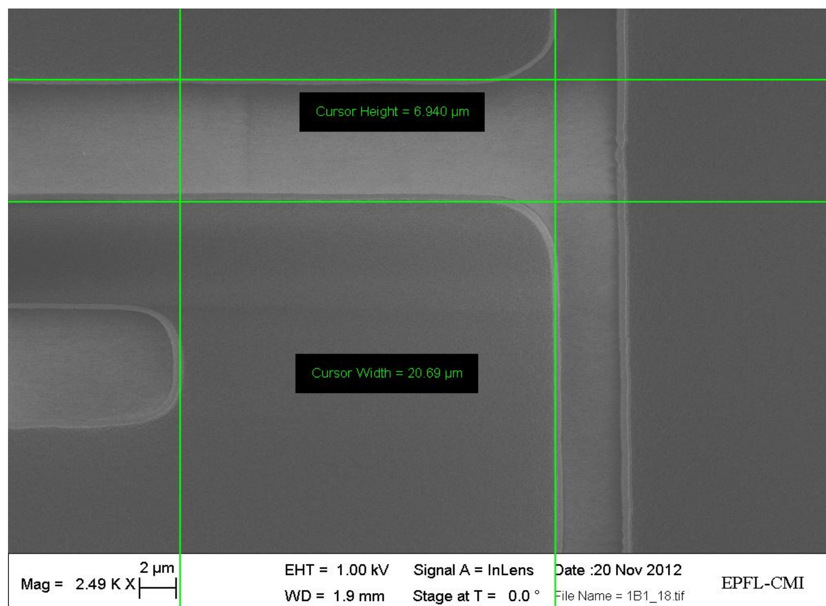


**Figure B.9:** Force sensor finger top view, Si test wafer

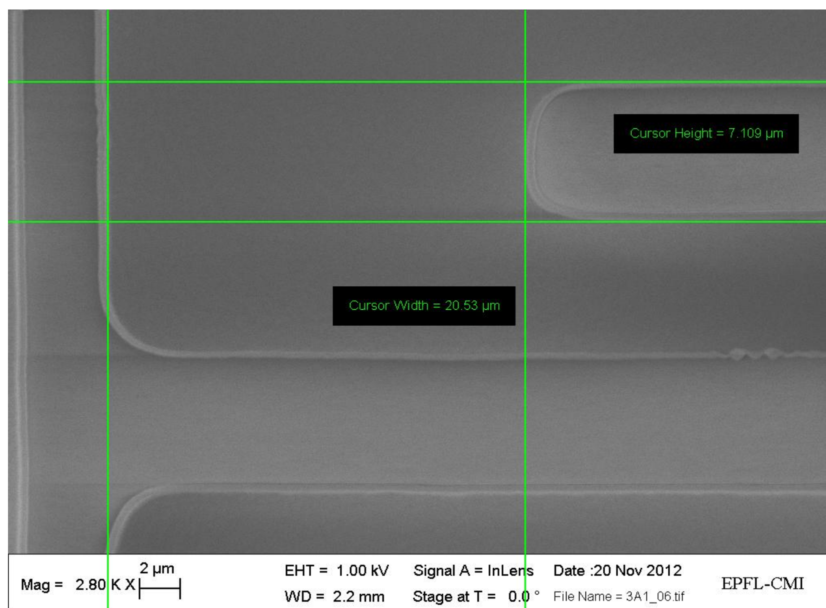


**Figure B.10:** Force sensor finger top view, Si test wafer

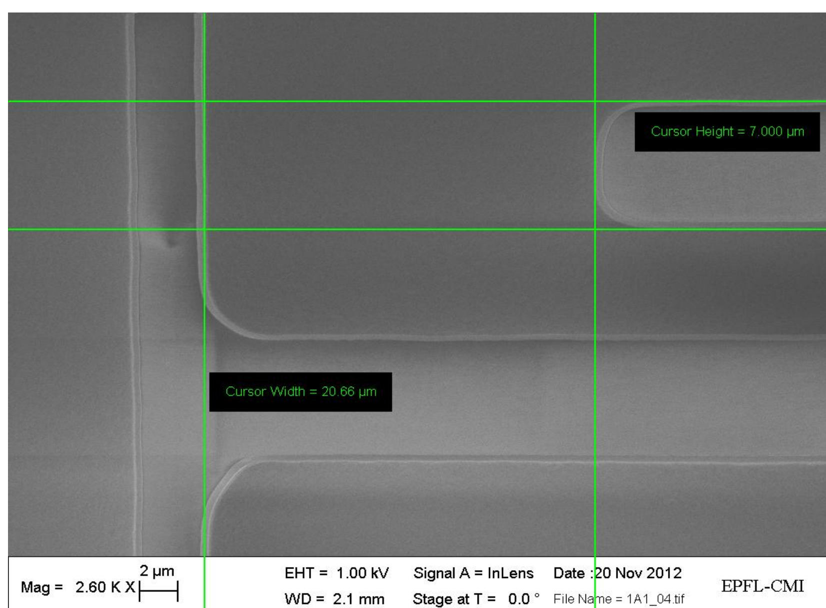


**Figure B.11:** Force sensor finger top view, Si test wafer

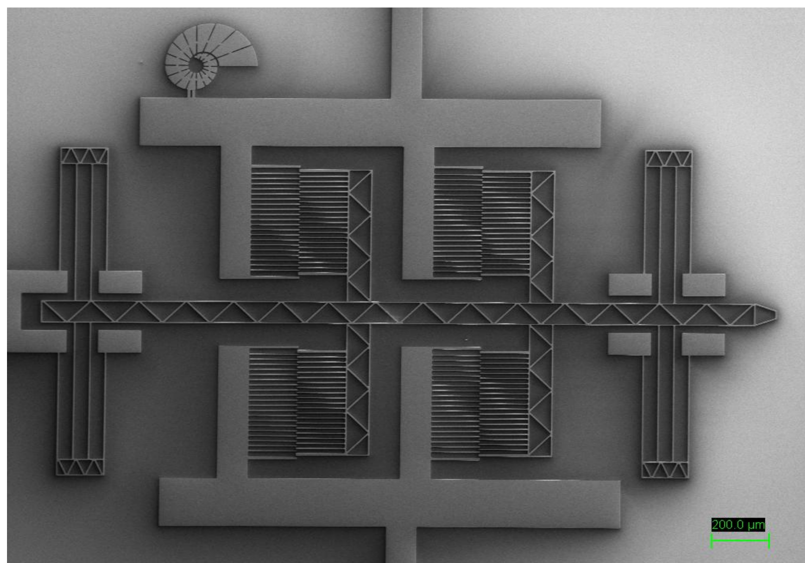


**Figure B.12:** Actuator of nanowire 1

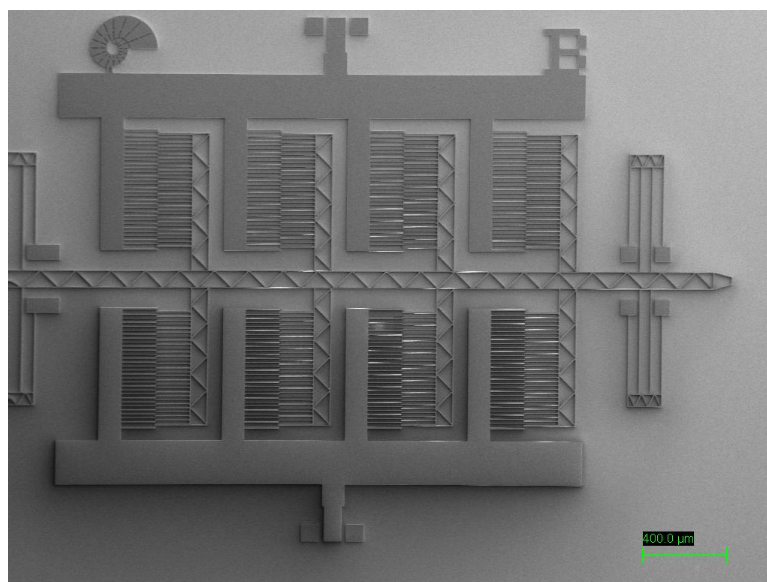


**Figure B.13:** Actuator of nanowire 2

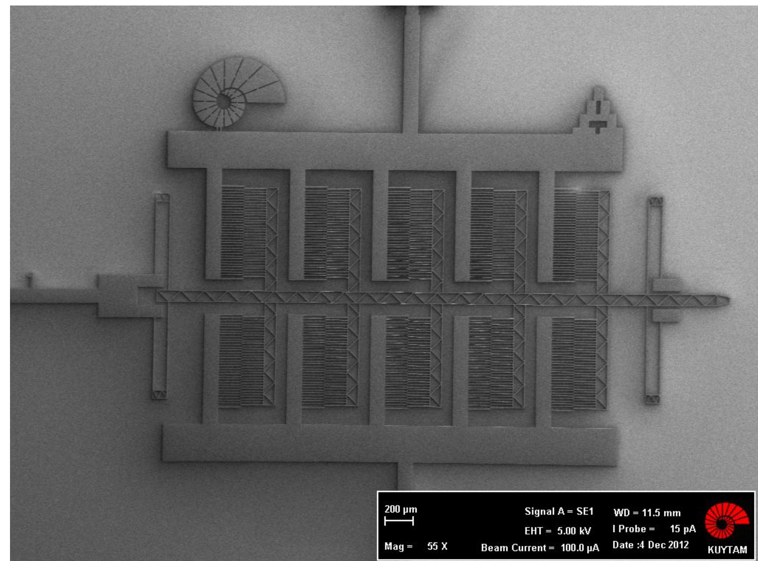


**Figure B.14:** Actuator of nanowire 3

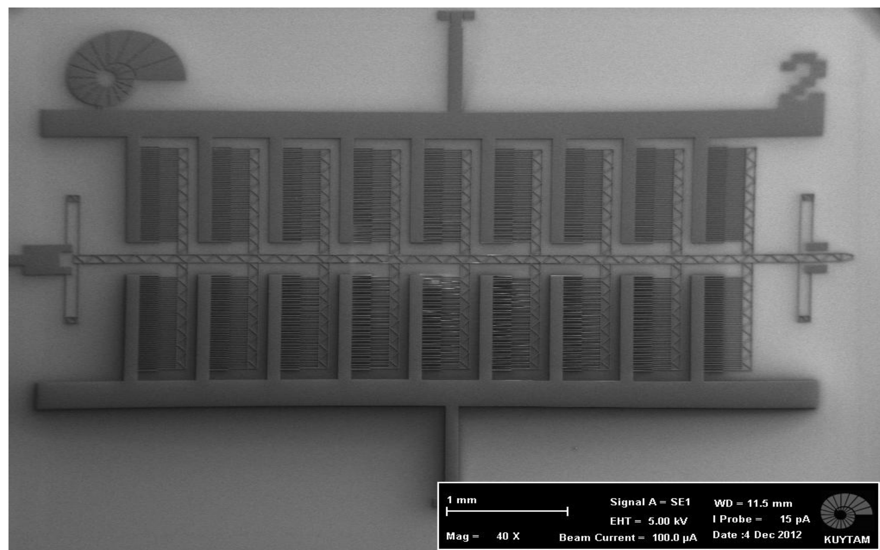


**Figure B.15:** Actuator of nanowire 4

# Appendix C

## ACTUATOR AND FORCE SENSOR LAYOUTS

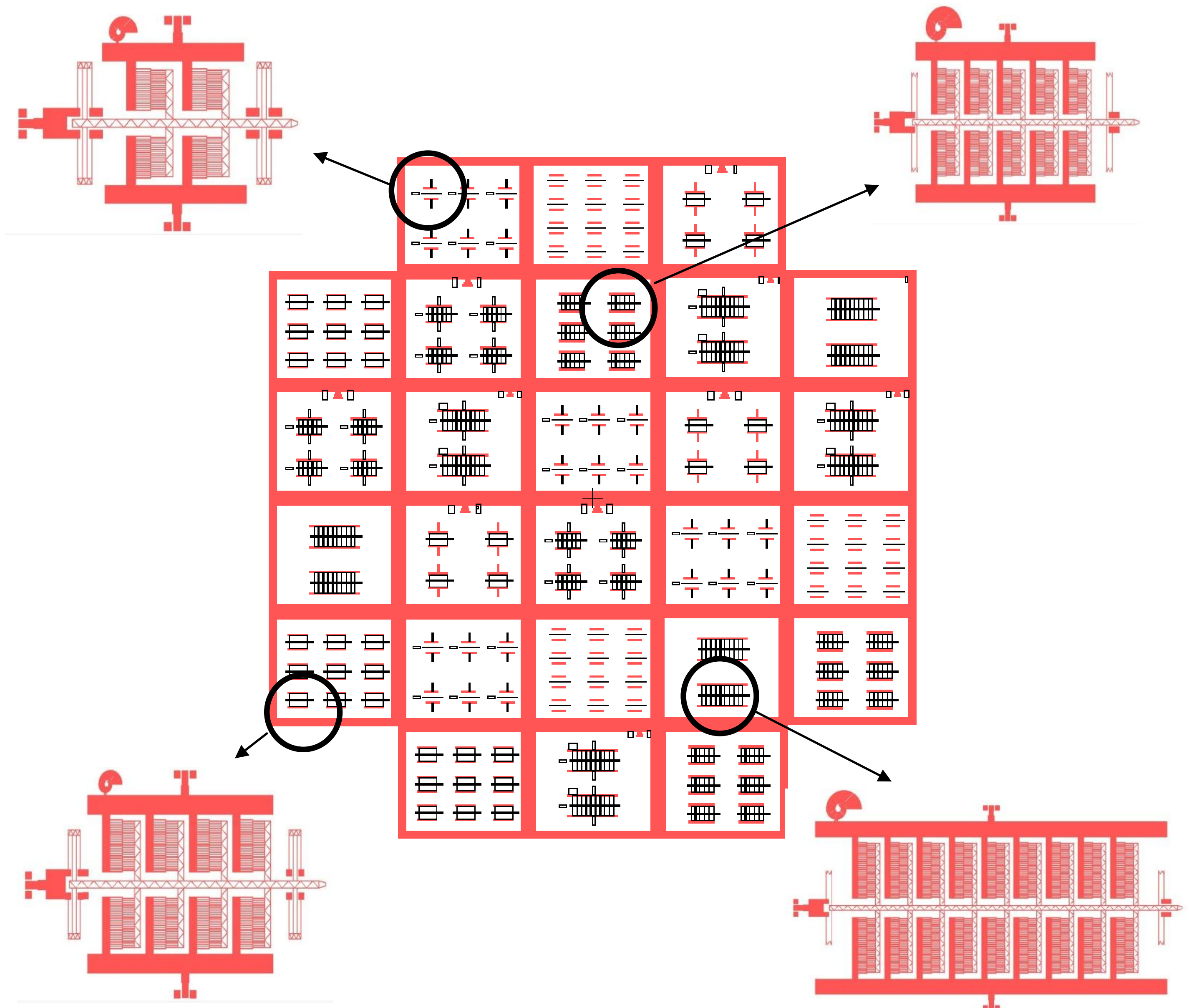

**Figure C.1:** First-generation actuator layout

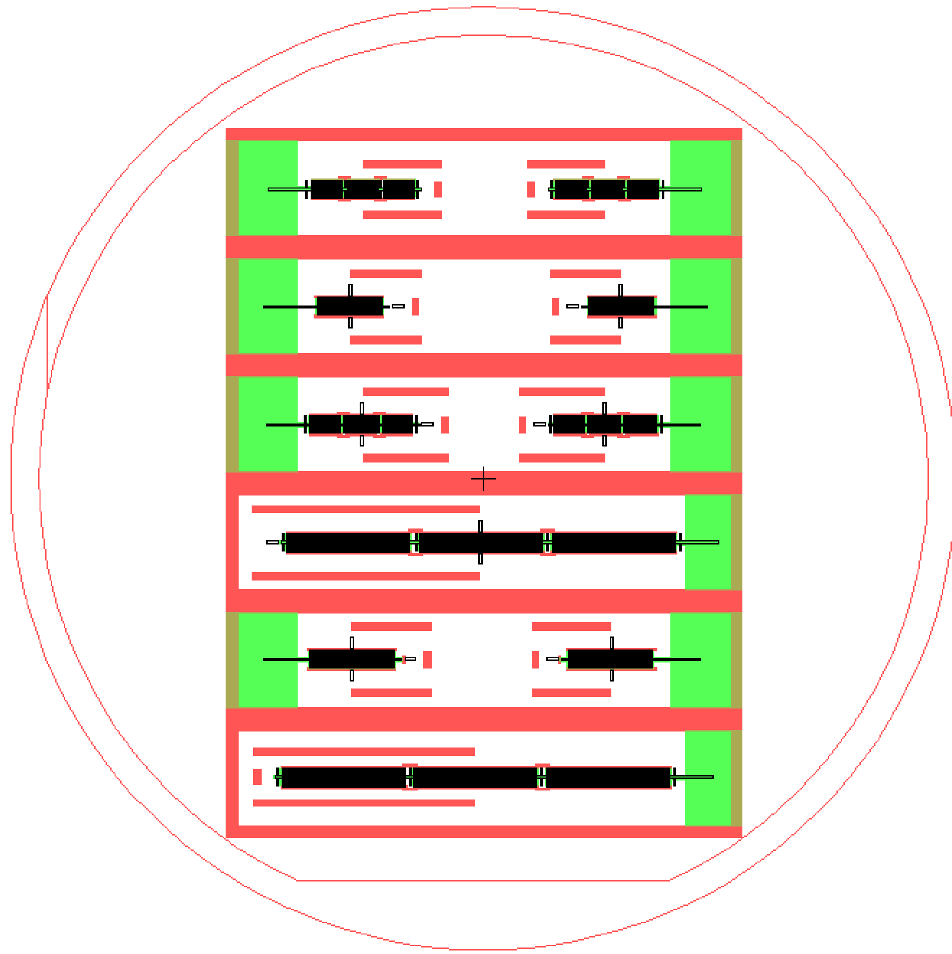

**Figure C.2:** First-generation force sensor layout

# Appendix D

## 2-D SIMULATIONS

### D.1. Actuator

**Table D.1:** Simulated actuator design parameters

| Samples | $w_{AC}$ [μm] | h [μm] | $g_x$ [μm] | $g_y$ [μm] | $k_{AC}$ [N/m] | Applied Voltage [V] | $N_{AC}$ |
|---|---|---|---|---|---|---|---|
| Nw 1 | 5 | 5 | 155 | 4 | 10 | 40 | 83 |

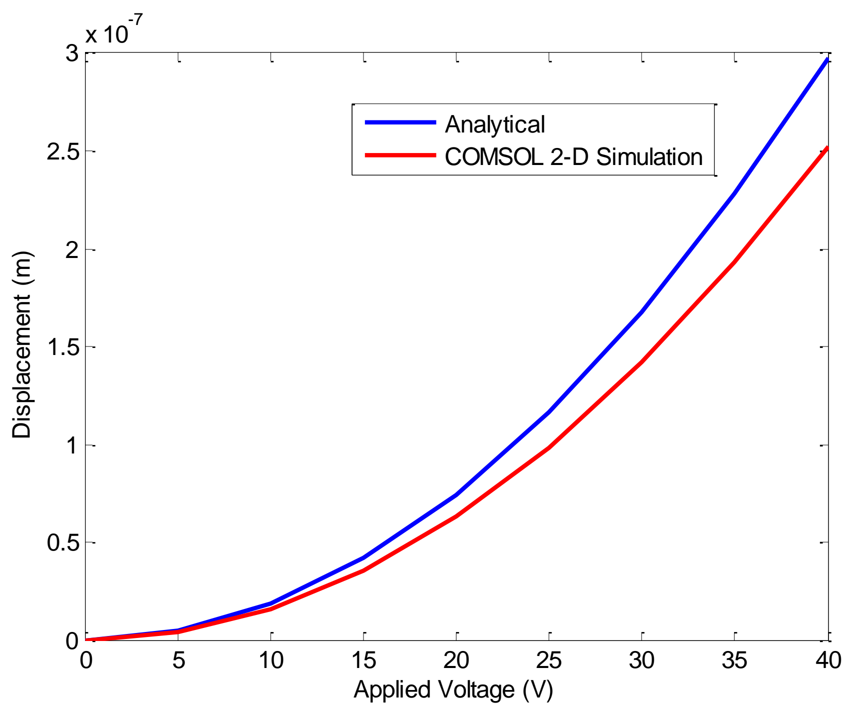


**Figure D.1:** Applied Voltage - Displacement plot of the 1st-generation actuator which is designed for 1st Si nanowire sample

40V is the maximum operation voltage for the 1st-generation actuators of all Si nanowires listed in Table 1.1. In order to understand the tendency of our approach we carried out 2-D simulation of the 1st actuator whose information is given in Table D.1 by using COMSOL Multiphysics 4.3a, Electromechanics (emi) module. Maximum displacement expected for actuator is calculated as 300nm and 2-D simulation gives a displacement value of 250nm at 40V resulting with an error of 17% (Figure D.1).

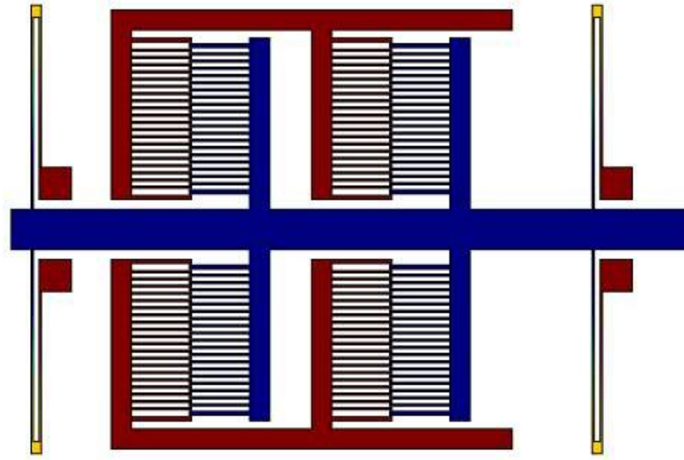

**Figure D.2:** Displacement profile of the 1st-generation actuator which is designed for 1st Si nanowire sample. Blue parts have the maximum displacement and dark red areas indicate fixed parts.

### D.2. Force Sensor

**Table D.2:** Simulated force sensor design parameters

| Samples | $w_{FS}$ [μm] | $l_{FS}$ [μm] | $d_1$ [μm] | $d_2$ [μm] | $k_{FS}$ [N/m] | Applied Voltage [$V_{FS}$] | Sensitivity [V/(μm/μm)] | $N_{FS}$ |
|---|---|---|---|---|---|---|---|---|
| Nw 4 | 8 | 750 | 5 | 30 | 20 | 2 | 7.34 | 136 |

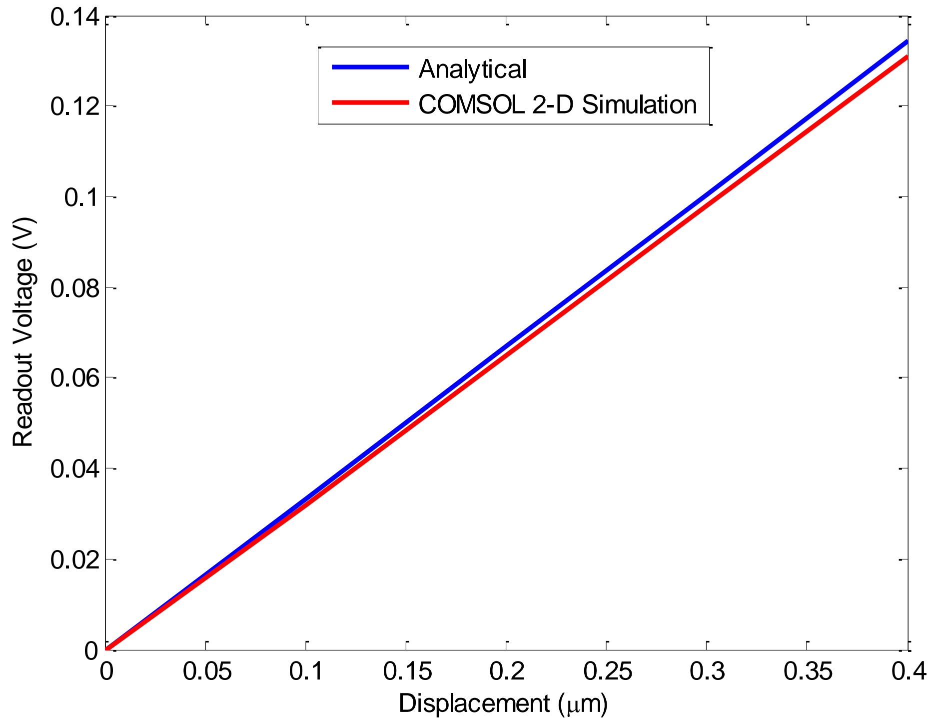


**Figure D.3:** Applied Voltage - Displacement plot of the 1st-generation actuator which is designed for 1st Si nanowire sample

Due to the computer RAM issues, the force sensor having minimum required area is simulated with COMSOL Multiphysics 4.3a, Electromechanics (emi) module. 1st-generation force sensor for the nanowire no. 4 is simulated (Figure D.3). Simulation is carried out for a maximum shuttle displacement of 400nm which is very close to the expected displacement. Examining Figure D.3, it is seen that readout voltage values for analytical expectation and 2-D simulation are almost same so that we conclude that our assumptions for designing a force sensor are correct. In Figure D.4, surface electric potential of the simulated force sensor can be seen.

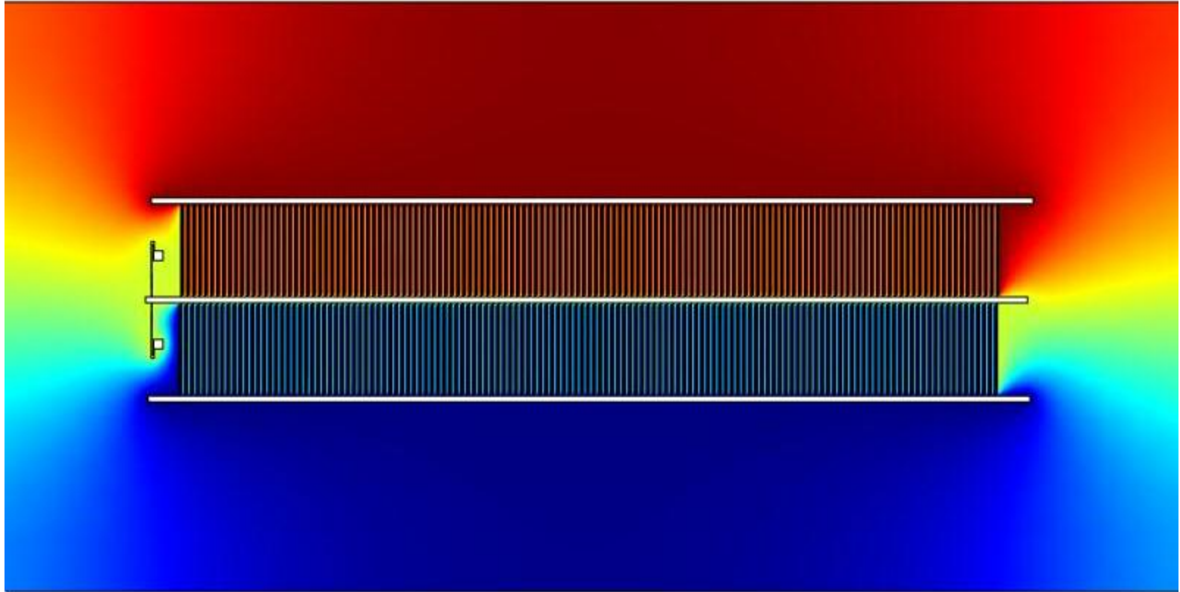

**Figure D.4:** Surface electric potential profile of the 1st-generation force sensor which is designed for 4th Si nanowire. Blue parts indicate a voltage value close to -2V and red areas demonstrate 2V regions. Other colors represent the voltage values between -2V and 2V.

**BIBLIOGRAPHY**

[1] Y.J. Kim, K. Son, I.C. Choi, I.S. Choi, W.I. Park, J.I. Jang, Adv. Funct. Mater., 21 (2011) 279-286.

[2] S. Hoffmann, I. Utke, B. Moser, J. Michler, S.H. Christiansen, V. Schmidt, S. Senz, P. Werner, U. Gosele, C. Ballif, Nano Letters, 6 (2006) 622-625.

[3] H. Ni, X.D. Li, H.S. Gao, Applied Physics Letters, 88 (2006) 3.

[4] J. Song, X. Wang, E. Riedo, Z.L. Wang, Nano Lett., 5 (2005) 1954-1958.

[5] H. Ni, X.D. Li, Nanotechnology, 17 (2006) 3591-3597.

[6] S. Hoffmann, F. Ostlund, J. Michler, H.J. Fan, M. Zacharias, S.H. Christiansen, C. Ballif, Nanotechnology, 18 (2007) 5.

[7] M.P. Manoharan, A.V. Desai, G. Neely, M.A. Haque, J. Nanomaterials, 2008 (2008) 1-7.

[8] D.F. Zhang, J.M. Breguet, R. Clavel, V. Sivakov, S. Christiansen, J. Michler, J. Microelectromech. Syst., 19 (2010) 663-674.

[9] Q.H. Jin, Y.L. Wang, T. Li, X.X. Li, F.F. Xu, Sci. China Ser. E-Technol. Sci., 51 (2008) 1491-1496.

[10] Q.H. Jin, T. Li, Y.L. Wang, X.X. Li, P. Zhou, F.F. Xu, in: IEEE Sensors, 2008.

[11] Y. Zhu, A. Corigliano, H.D. Espinosa, J. Micromech. Microeng., 16 (2006) 242-253.

[12] H.D. Espinosa, Y. Zhu, N. Moldovan, J. Microelectromech. Syst., 16 (2007) 1219-1231.

[13] D.F. Zhang, J.M. Breguet, R. Clavel, L. Philippe, I. Utke, J. Michler, Nanotechnology, 20 (2009) 7.

[14] M. Naraghi, T. Ozkan, I. Chasiotis, S.S. Hazra, M.P. de Boer, J. Micromech. Microeng., 20 (2010) 9.

[15] M. Kiuchi, S. Matsui, Y. Isono, J. Microelectromech. Syst., 16 (2007) 191-201.

[16] B. Pant, B.L. Allen, T. Zhu, K. Gall, O.N. Pierron, Applied Physics Letters, 98 (2011) 3.

[17] J.J. Brown, A.I. Baca, K.A. Bertness, D.A. Dikin, R.S. Ruoff, V.M. Bright, Sens.

[18] G.C. Johnson, P.T. Jones, R.T. Howe, in: Conference on Micromachining and Microfabrication Process Technology V, Spie-Int Soc Optical Engineering, Santa Clara, Ca, 1999, pp. 94-101.

[19] D. Zhang, in, Ecole Polytechnique Federale De Lausanne, 2010. 84

[20] D.J. Bell, T.J. Lu, N.A. Fleck, S.M. Spearing, J. Micromech. Microeng., 15 (2005) S153-S164

[21] B. Gumus, in, Koç University, 2012.

[22] E.F. Arkan, in, Koç University, 2011.

[23] O. Sardan, in, Koç University, 2006.

[24] Micro Electronics Processing Tech., 6.152J / 3.155J, 2004

.

# VITA

Gökhan Nadar was born in Eskişehir, Turkey on April 4th, 1988. He is graduated from Eskişehir Anatolian High School in Eskişehir, Turkey, in June 2006. He received his B. Sc. from the Department of Mechanical Engineering at Koç University, Istanbul, Turkey, in June 2011. He started M. Sc. program at the Department of Mechanical Engineering at Koç University in September 2011 in Assoc. Prof B. Erdem Alaca's research group. Completing his M. Sc studies, Gökhan plans to enroll in PhD program to architect further studies.